1 **Revision 1**

2 **Pyrite geochemistry in a porphyry-skarn Cu (Au) system and implications for ore**
3 **formation and prospecting: Perspective from Xinqiao deposit, Eastern China**

4

5 Xin Xiao[1, 2, 3], Taofa Zhou[1, 3*], Pete Hollings[1, 4], Noel C. White[1, 3, 5], Yu Fan[1, 3], Lejun Zhang[5],
6 Bin Fu[6]

7 [1]*Ore Deposit and Exploration Centre (ODEC), School of Resources and Environmental*
8 *Engineering, Hefei University of Technology, Hefei 230009, China*

9 [2] *School of Earth Resources, China University of Geosciences, Wuhan 430074, China*

10 [3]*Anhui Province Engineering Research Center for Mineral Resources and Mine Environments,*
11 *Hefei 230009, China*

12 [4]*Department of Geology, Lakehead University, 955 Oliver Road, Thunder Bay, Ontario P7B*
13 *5E1, Canada*

14 [5]*Centre for Ore Deposit and Earth Sciences (CODES), University of Tasmania, Private Bag*
15 *79, Hobart, Tasmania 7001, Australia*

16 [6]*Research School of Earth Sciences, The Australian National University, Canberra, ACT 2601,*
17 *Australia*

18 *Corresponding author

19 E-mail address: tfzhou@hfut.edu.cn

20

Abstract

Stratabound ore has been recognized as an end member of porphyry copper systems, but pyrite chemistry has not been widely applied to linking stratabound ore with the related porphyry and skarn system. Stratabound ore is commonly developed around porphyry-skarn systems in eastern China, and is characterized by abundant colloform pyrite; however the origin of the colloform pyrite has been contentious. Xinqiao deposit is ideal for study of pyrite geology and geochemistry with the aim of elucidating formation of the stratabound ore and to decipher the evolution of pyrite compositions in a porphyry-skarn environment. The colloform pyrite paragenesis and S isotopes indicate that it formed during early skarn mineralization, based on its occurrence in stockwork veins cutting skarn minerals, and that it is replaced by later hypogene sulfides; the $\delta^{34}S$ of colloform pyrite (average 6.12‰) is close to the $\delta^{34}S$ value of both porphyry- (average 5.06‰) and skarn-type pyrite (average 4.65‰). The colloform texture formed as an aggregate of nanometer- or micrometer-sized (< 0.2 μm) pyrite cubes produced by rapid crystallization from a high fS_2, low temperature, and supersaturated fluid. Supersaturation of the fluid was probably produced by rapid decompression that triggered fluid boiling and cooling when the magmatic-hydrothermal fluid (derived from Cretaceous magma) flowed along the Devonian-Carboniferous unconformity. Subsequently, the colloform pyrite was replaced by later stage pyrite with distinctive trace elements (Co, Ni and Se), indicating that the stratabound ore at Xinqiao formed from multiple pulses of magmatic-hydrothermal fluids derived from an Early Cretaceous stock.

Cobalt, Ni and Se enrichment in porphyry- and proximal skarn-type pyrite suggests they formed at relatively high temperature, whereas the colloform pyrite shows trace element

contents (Cu, Pb, Zn, Ag and Bi) similar to those in distal skarn pyrite, suggesting that they may have formed in the same fluid environment. The trace element variations in pyrite from stratabound, skarn and porphyry ore probably resulted from decreasing fluid temperature and increasing pH away from the source. Our data, combined with previous studies, show that Co and Ni in pyrite increase towards porphyry and skarn ore, whereas As, Sb, Pb, Ag and Bi are enriched in pyrite in distal stratabound ore, which extends for 1-2 km away from the intrusion. A plot of As/Se versus Co discriminates the three ore types that occur associated with porphyry-skarn Cu systems in the Middle and Lower Yangtze belt (MLYB). These results indicate pyrite chemistry can be effective in discriminating the genesis of different deposit types related to porphyry-skarn systems and can potentially be used as a vectoring tool during exploration in the MLYB and elsewhere.

Keywords: Colloform pyrite, Stratabound ore, Pyrite geochemistry, Porphyry-skarn deposit, The Middle–Lower Yangtze River metallogenic belt

Introduction

Stratabound massive sulfide ore has been recognized in a variety of deposit types, such as sedimentary exhalative deposit (SEDEX), volcanic hosted massive sulfide (VHMS), and Manto-type skarns, or as distal deposits associated with porphyry copper deposits (Laznicka et al. 1981; Meinert 1982; Fontboté et al. 1990; Sillitoe 2010). It is also widespread in the Middle-Lower Yangtze River metallogenic belt (MLYB), and as the most important resource of copper, gold and sulfur in eastern China, it has been the subject of abundant research and exploration during the past 40 years (Fig. 1; Chang et al. 1991; Mao et al. 2020). Stratabound

sulfide ore in the MLYB is restricted to stratigraphic horizons that overlie the unconformity between Devonian sandstone and Carboniferous carbonate units (Fig. 2). A ubiquitous feature of the stratabound ore is the presence of abundant colloform pyrite, which has been interpreted to have formed either by Carboniferous syn-sedimentary processes (Xie et al. 2014; Xu et al. 2020) or seafloor exhalative sedimentation (Gu et al. 2000). However, the stratabound sulfide ores occur close to early Cretaceous porphyry-skarn systems, leading other studies to conclude that initial syn-sedimentary or seafloor exhalative deposits may have been overprinted by Cretaceous magmatic-hydrothermal fluids (Xu and Zhou 2001; Gu et al. 2007; Zhou et al. 2010; Guo et al. 2011), or that the deposits are solely related to Cretaceous magmatism (Pan and Dong 1999; Mao et al. 2011; Zhang et al. 2017; Li et al. 2018, 2019).

Pyrite is a dominate constituent of stratabound ore in the MLYB and has distinctive textures (e.g., colloform pyrite and subhedral-euhedral pyrite). There have been extensive studies on the mineralogy, morphology, trace elements, and isotopes of pyrite from stratabound ores (Zhou et al. 2010; Guo et al. 2011; Zhang et al. 2017; Li et al. 2017, 2018; Xu et al. 2020), but the origin and genesis of the colloform pyrite is still debated. In addition, stratabound sulfide ore is generally distributed around early Cretaceous porphyry-skarn systems, and pyrite is also widespread in porphyry and skarn ore. Although, stratabound ore has been recognized as an end member of porphyry copper systems (Sillitoe 2010), pyrite chemistry has not been widely applied to linking stratabound ore with their related porphyry and skarn systems.

Xinqiao deposit in Tongling district was selected for study, based on (Fig. 1B): 1) it hosts the largest stratabound ore in the MLYB, with mineralized horizons extending for 2600 m

horizontally and 1810 m vertically, with an average thickness of 21 m (e.g., Fig. 2; Chang et al. 1991; Pan and Dong 1999); 2) the colloform pyrite is well preserved, and developed multiple-stages of pyrite in the stratabound ore; 3) skarn and porphyry ore also contribute important copper and gold reserves at Xinqiao (e.g., Fig. 2; Chang et al. 1991; Tang et al. 1998; Xiao et al. 2021). These features make Xinqiao is an ideal target for studying the formation of stratabound ore in porphyry-skarn systems, and to determine systematic geochemical variations in pyrite from stratabound, skarn and porphyry ore. In this paper, we present new geological observations of the textures and paragenesis of colloform pyrite, in situ trace element data for pyrite and S isotopes of sulfides from the stratabound, skarn and porphyry ore, and S isotopes of regional sedimentary pyrite. Our results highlight: 1) the magmatic-hydrothermal origin of colloform pyrite; 2) the multi-stage formation of the stratabound ore; and 3) that pyrite chemistry (Co, Ni, As, Sb, Pb, Ag and Bi) can vector from stratabound ore to skarn and porphyry ore.

Geological setting

The MLYB is the one of the most important producers of copper, iron, and gold in China, and has been extensively studied and explored during the past 60 years (Chang et al. 1991; Zhou et al. 2015; Mao et al. 2011, 2020). The MLYB occurs between the Yangtze Block (to the south), the North China Block (to the north) and the Triassic Qinling-Dabieshan Ultra-High Pressure Belt (to the northwest). The boundaries of the MLYB are the Xiangfan-Guangji (XGF), Tan-Lu (TLF) and Chongyang-Changzhou faults (CCF) (Figs. 1A, B; Chang et al. 1991; Pan and Dong 1999). The regional stratigraphy consists of Archean to

Late Proterozoic metamorphic basement rocks, Cambrian to Early Triassic submarine sedimentary rocks, and thick sequences of Middle Triassic terrestrial sedimentary and volcanic rocks (Chang et al. 1991). The main tectonic framework developed in the Middle Triassic and comprises a series of faulted uplifted and depressed zones that control the distribution of magmatic rocks and ore deposits (Pan and Dong 1999; Mao et al. 2011). A total of 200 Fe-Cu-Au polymetallic ore deposits have been recognized in the MLYB, including magnetite-apatite, porphyry, skarn and stratabound Cu-Fe-Au deposits that cluster in seven districts (from west to east Edong, Jiurui, Anqing-Guichi, Luzong, Tongling, Ningwu and Ningzhen (Fig. 1B; Chang et al. 1991; Pan and Dong 1999). There have been three related magmatic and metallogenic events in the MLYB: Cu-Au mineralization formed at 148-135 Ma, mainly in porphyry, skarn, and strata-bound deposits associated with high-K calc-alkaline dioritic or granodioritic intrusions; Fe mineralization mainly formed at 135-123 Ma with calc-alkaline dioritic intrusions; and minor uranium-gold mineralization formed at 127-123 Ma with A-type granitoids (Tang et al. 1998; Zhou et al. 2010; Mao et al. 2011).

The Tongling district is located in the center of the MLYB and contains many Cu-Au (Fe) deposits (Figs. 1B, C). The copper and gold resources mainly occur in stratabound, skarn, and porphyry ore deposits, with Silurian to Middle Triassic marine sedimentary rocks being the main host rocks for the ore deposits. Mesozoic intrusions (granodiorite, pyroxene diorite, quartz diorite) and Cu-Au (Fe) deposits are mainly associated with NE-trending folds and a series of NE-, NNE-, NW-, and NNW-trending faults (Fig. 1C; Tang et al. 1998). The stratabound sulfide ores in the Tongling district are commonly associated with skarn and porphyry ore deposits, which is an unusual association when compared with global

porphyry-skarn Cu-Au deposits. The stratabound sulfide ore is the most economically significant ore type at Xinqiao, Dongguashan, and Tianmashan, and is present to a minor extent in the Tongguanshan skarn Cu-Au deposit (Fig. 1C, Tang et al. 1998).

Deposit geology

The stratigraphic units exposed near the Xinqiao deposit range from Middle–Upper Silurian to Lower Triassic, but lack Lower to Middle Devonian rocks (Fig. 2). Silurian and late Devonian formations predominantly consist of sandstone, and occur as the footwall to the stratabound sulfide ore. Carboniferous units consist of silty shale, sandstone and siltstone, overlain by thick limestone or dolomitic limestone, and form the hanging wall to the stratabound ore. The overlying Permian stratigraphy is widespread at Xinqiao, with a total thickness of more than 400 m. It consists of limestone interbedded with sandstone and siltstone. The Xinqiao deposit is located at the intersection of the NE-trending Dachengshan anticline and the NNE-trending Shenchong syncline (Xu and Gu 2001). These structures influenced the location of both the magmatic intrusions and the orebodies. A quartz monzodiorite (the Jitou Stock) outcrops over 1.2 km^2 where it intruded into sedimentary rocks, and is closely associated with skarn and porphyry mineralization (Xiao et al. 2021). SHRIMP zircon U-Pb dating of the quartz monzodiorite yielded an age of 140.4 ± 2.2 Ma (Wang et al. 2004).

The Xinqiao deposit consists of one large and several small orebodies, with estimated metal reserves of >0.5 Mt Cu @ 0.71%, 11.2 t Au @ 4.7g/t, 25 Mt Fe @ 46%, plus Pb and Zn by-products (Xu and Zhou 2001; Zhang et al. 2020). The main orebody is stratabound and

153 extends along the unconformity surface between Devonian sandstone and Carboniferous
154 carbonate units (Figs. 2A, B); locally the orebody intrudes into the hanging wall limestone
155 (Pan and Dong 1999; Li et al. 2017). The stratabound ore extends for 2600 m horizontally,
156 and 1810 m vertically, with an average thickness of 21 m, and locally, close to the quartz
157 monzodiorite intrusion, can be more than 70 m thick (Xu and Gu 2001). The stratabound ore
158 is the main economic resource at Xinqiao, and contains >70% of the copper, gold, and sulfur
159 reserve (Chang et al. 1991). It consists of dark-grey colloform pyrite ore and massive
160 coarse-grained pyrite ore (Figs. 3A, B). The colloform pyrite ore mainly occurs in the
161 southwest part of the stratabound ore and has a sharp contact with massive pyrite (Xu and
162 Zhou 2001; Li et al. 2019). The sulfide ores are massive or laminated in texture, and are
163 composed of pyrite (>60%), chalcopyrite (20%) and quartz (15%), with minor calcite and
164 siderite (Figs. 3A, B).

165 The skarn orebodies closely follow the contact between the intrusion and the host
166 limestones (Fig. 2B) and are composed of massive or disseminated pyrite, chalcopyrite, and
167 magnetite (Figs. 3C, D). Recent drilling indicates that the porphyry copper-gold
168 mineralization at Xinqiao is generally hosted in quartz-pyrite-chalcopyrite stockwork veins or
169 disseminated in the deeper parts of the Jitou stock with average Cu grade 0.3~0.6 wt% (Figs.
170 2B and 3E-F; Xiao et al. 2021). In general, the stratabound orebody shows weak alteration
171 and replacement by hematite, siderite, quartz and calcite with silicic and sericitic alteration
172 developed in the footwall to the stratabound ore (Li et al. 2017; Zhang et al. 2017). In the
173 skarn ore zone there is strong retrograde alteration with epidote-chlorite or
174 chlorite-pyrite-calcite veins replacing the garnet skarn (Xiao et al. 2018). The porphyry ore at

This is the peer-reviewed, final accepted version for American Mineralogist, published by the Mineralogical Society of America.
The published version is subject to change. Cite as Authors (Year) Title. American Mineralogist, in press.
DOI: https://doi.org/10.2138/am-2022-8527. http://www.minsocam.org/

Xinqiao displays characteristic porphyry-style alteration, with a potassic core surrounded by a phyllic zone with a poorly developed outer zone of propylitic alteration (Fig. 2B). Phyllic alteration is widely developed and contains quartz-pyrite-chalcopyrite veins (Fig. 3E). The potassic alteration zone is characterized by quartz-chalcopyrite-pyrite veins and veinlets (Fig. 3F).

Samples and analytical methods

Sampling

To constrain the metal source and genesis of the stratabound ore in Xinqiao deposit, seventeen samples were selected for this study. Four samples were from outcrops of unmineralized sedimentary formations that are the main host rocks of the stratabound ore (Fig. 1C), including the late Devonian Wutong Formation (D_3w), early Carboniferous Gaolishan Formation (C_1g), late Carboniferous Chuanshan Formation (C_2c) and early Permian Qixia Formation (P_1q) (Fig. 4). Thirteen samples were from Xinqiao drill core, open pit and underground mine (Fig. 2), and included stratabound ore (dark-grey colloform pyrite ore; Figs. 3A and 7; massive coarse pyrite ore; Fig. 3B), skarn ore (distal magnetite-pyrite-calcite ore; Fig. 3C; proximal massive pyrite-chalcopyrite ore; Figs. 3D and 7A) and porphyry ore (quartz-pyrite-chalcopyrite veins with muscovite halos; Fig. 3E; quartz-pyrite-chalcopyrite veins where K-feldspar mainly occurs as veinlets or vein halos; Fig. 3F). All samples were mounted in epoxy resin pucks and polished.

Methods

NaClO etching of pyrite

Polished mounts were etched using sodium hypochlorite solution (6–14% w/v active chlorine; NaOCl) to reveal pyrite internal textures. NaOCl was dropped on the sample surface and left for periods of 1 to 2 minutes, until the color of the pyrite changed, then rinsed immediately with cold tap water and dried (Sykora et al. 2018).

SEM and EDS analysis

Detailed investigation of the morphology of pyrite was performed using a Hitachi SU-70 scanning electron microscope (SEM) at the University of Tasmania. Secondary-electron mode was used at 3-5 kV to observe the surface structure of colloform pyrite and at higher voltages (20 kV) for high resolution imaging. BSE images and energy-dispersive X-ray spectroscopy (EDS) at 15 kV was used to measure the chemical composition of the pyrite.

Micro-Raman spectroscopy

Micro-Raman spectroscopic analyses of stratabound ore samples were carried out using a WITec alpha300-R confocal Raman system coupled with a Peltier cooled EMCCD detector at the State Key Laboratory of Biogeology and Environmental Geology, China University of Geosciences (Wuhan). The instrument was equipped with a 532-nm wavelength laser and set at a power of 5 mW. Raman spectra were obtained at magnifications of 50×(N.A.=0.75) and with a focus spot size of 1μm. The Raman spectra were collected in the 0–3500 cm^{-1} range using 600 lines per millimeter grating, which yielded a spectral resolution of 4 cm^{-1}.

LA-ICP-MS (laser ablation-inductively coupled plasma-mass spectrometry)

Trace element analyses and mapping of representative pyrite grains from Xinqiao was done using laser ablation-inductively coupled plasma-mass spectrometry (LA-ICP-MS) at the Centre for Ore Deposit and Earth Sciences (CODES), University of Tasmania, Australia,

using an Agilent 7700 quadrupole ICP-MS coupled with a 193 nm Coherent Ar-F excimer laser and an ASI Resolution S155 ablation cell. Trace element analyses were performed with a uniform spot diameter of 29 μm at 5 Hz with energy of 3.0 J/cm^2 in a helium atmosphere flowing at 0.35 L/min, mixed with argon flowing at 1.05 L/min immediately after the ablation for 60s after measuring the gas blank for 30s. STDGL2b2, GSD-1G and Peru Py were used as primary standards (Jochum et al. 2005; Danyushevsky et al. 2011). The in-house software (CODES, UTAS; unpublished) was employed for data reduction. Thirty-six trace elements were measured in pyrite but only 14 elements (Co, Ni, Cu, Zn, As, Se, Ag, Sb, Te, W, Au, Tl, Pb and Bi) are presented in this paper, as these elements were consistently above the detection limit and displayed significant variability in different pyrite grains (Fig. 10). Trace element mapping was conducted under similar conditions with a 9 μm spot size and 10 Hz pulse rate at an ablation speed of 6 μm/s. Detailed descriptions of the laser mapping and spot analysis methodology are given in Large et al. (2009) and Gregory et al. (2016).

SHRIMP-SI (Sensitive high-resolution ion-micro-probe-Stable isotope)

In situ sulfur isotopes of selected pyrite grains from regional sedimentary rocks and sulfides (pyrite, pyrrhotite and chalcopyrite) from Xinqiao were measured using the SHRIMP SI at the Research School of Earth Sciences, Australian National University (RSES, ANU) (Ireland et al. 2008; Tanner et al. 2016), utilizing a spot diameter of 10μm for pyrite, pyrrhotite and chalcopyrite. Detailed descriptions of the methodology are presented by Ireland et al. (2014) and Philippot et al. (2018). Ruttan pyrite ($\delta^{34}S_{V\text{-}CDT}$ value of +1.2‰, Crowe and Vaughan 1996) was the primary standard used to normalize the pyrite sulfur isotope data; the sulfur isotope data of chalcopyrite and pyrrhotite were normalized using

This is the peer-reviewed, final accepted version for American Mineralogist, published by the Mineralogical Society of America.
The published version is subject to change. Cite as Authors (Year) Title. American Mineralogist, in press.
DOI: https://doi.org/10.2138/am-2022-8527. http://www.minsocam.org/

241 Norilsk chalcopyrite ($\delta^{34}S_{V\text{-}CDT}$ value of +8.0‰) and Anderson pyrrhotite ($\delta^{34}S_{V\text{-}CDT}$ value of
242 +1.4‰) respectively (Crowe and Vaughan 1996). Analyses of reference materials were
243 performed after every three or four sample analyses.
244
245 **Results**
246 **Pyrite petrology and morphology**
247 Pyrite is dispersed and commonly occurs disseminated in regional sedimentary rocks and
248 does not show internal textures (Fig. 4). Pyrite disseminated in Permian carbonaceous
249 limestone (Qixia Formation, P_1q-Py) is typically fine-grained (50-100 μm) with euhedral and
250 subhedral crystals (Figs. 4A, B). Subhedral fine-grained pyrite (50-100 μm) occurs as clusters
251 in Carboniferous limestone/dolomite (Chuanshan Formation, C_2c-Py; Figs. 4C, D). The pyrite
252 in Carboniferous silty shale (Gaolishan Formation, C_1g-Py; Figs. 4E, F) is fine-grained (less
253 than 100 μm) and anhedral. In the Devonian sandstone (D_3w-Py) pyrite ranges from 50 to 300
254 μm in size and is euhedral (Figs. 4G, H).
255 Three types of pyrite can be identified in the stratabound sulfide ore (Py1/2/3) at Xinqiao
256 (Fig. 5). Py1 displays distinct colloform textures or aggregates in veins cutting pyrrhotite
257 (Figs. 5A, E and 7D-F) and magnetite (Figs. 7G, H). Scanning electron microscope imaging
258 and Raman results showed that the colloform zone consisted of aggregates of abundant
259 micron or nanometer (< 2 μm) sized cubic pyrite grains (Fig. 6); the changes of brightness
260 that cause the colloform texture are caused by variations in the grain size of the pyrite. Py2 is
261 coarse-grained (300 μm-2 mm), euhedral to subhedral and commonly replaces colloform
262 pyrite (Py1; Figs. 5A, C, D and 7). Medium- to fine-grained (50-400 μm) subhedral pyrite

(Py3) occurs with chalcopyrite and quartz as veins cutting Py2 and Py1 (Figs. 5A, B, E and 7). Pyrite4/4a from distal skarn ore can be recognized by its occurrence (Fig. 3C); Py4 is medium- to coarse-grained (200-500 μm) with sub-angular to sub-rounded edges, is disseminated with calcite, and is cut by fine-grained (50-100 μm) pyrite veins (Py4a, Figs. 3C and 5F). Py5 occurs in the massive pyrite-chalcopyrite ore from the proximal skarn zone (Fig. 3D) and is characterized by subhedral medium- to coarse-grained crystals (Fig. 5G). Py6 is from a quartz-pyrite vein with a muscovite halo from the phyllic alteration zone (Fig. 3E); the pyrite ranges in diameter from <300μm to 2mm and has angular to rounded edges (Fig. 5H). Py7 is subhedral and coarse-grained and is found in quartz-pyrite-chalcopyrite-molybdenite veins (Fig. 3F). NaOCl etching revealed strong oscillatory zoning in Py7 (Fig. 5I).

Trace element compositions of pyrite

A total of 213 spots on pyrite from Xinqiao deposit were measured by LA-ICP-MS; detailed results are reported in Appendix Table 1A and shown in Figure 10. LA-ICP-MS element mapping was conducted to characterize the distribution of trace elements in different textures of pyrite from Xinqiao deposit (Fig. 9).

The trace elements in pyrite from Xinqiao vary with the different types (Fig. 10). Py1 (colloform texture) contains high As, Cu, Pb and Ag with values between 100 and 1000 ppm (Pb is above 1000 ppm; Sb and Bi are between 10 and 100 ppm; Co, Ni, Se, and Te are less than 10 ppm; Au is near 0.1 ppm). Most trace elements in Py2 and Py3 are below 10 ppm, apart from As in Py2, which is above 500 ppm, and Py3 is enriched in Co (average 133 ppm). Py4 and Py4a have similar geochemistry with most trace elements ranging from 10 to 100

ppm, apart from Co (less than 1 ppm). However, Py4a has higher Cu (average is 1863 ppm) and Zn (average is 359 ppm) than the other pyrite types. Most trace elements in Py5 from the massive skarn-type pyrite-chalcopyrite ore have low trace element concentrations typically less than 10 ppm. Py6/7 from the porphyry ore is enriched in Co, Ni, and Se, with Py7 having the highest Co (164-2365 ppm) and Ni (25-740 ppm) concentrations, whereas other trace elements are less than 10 ppm (Fig. 10).

LA-ICP-MS mapping suggests that the trace elements in pyrite are part of the crystal lattice rather than occurring as inclusions (Fig. 9). Copper, Zn, Pb, Bi and Ag are concentrated in Py1 and are homogeneously distributed in bands (Figs. 9A, B); Py2 grains have higher As concentration (Fig. 9B), and Co is enriched in the cores of Py3 grains (Fig. 9A). Py7 grains from the porphyry ore display obvious oscillatory zoning of Co and Ni (Fig. 9C).

SHRIMP in situ sulfur isotopes

In situ SHRIMP sulfur isotope data for sulfides from Xinqiao (pyrite, pyrrhotite and chalcopyrite) and sedimentary rocks (pyrite) are shown in Appendix Table 2A and Figure 11. The $\delta^{34}S$ values of pyrite from the stratabound, skarn and porphyry ores are similar and fall in a narrow range with Py1 having $\delta^{34}S$ values of 3.21 - 8.58‰ (mean 6.12‰, n=28), Py2 displaying a narrow $\delta^{34}S$ range of 3.19-7.46‰ (n=15), and Py3 varying from 3.88 to 7.75‰ (n=14). The $\delta^{34}S$ values of Py4a, Py4 and Py5 from the skarn ore are 2.74-5.83‰ (n=7), 0.81-4.83‰ (n=6), 1.15-7.59 ‰ (n=8), respectively. Py6 and 7 from the porphyry ore has $\delta^{34}S$ values of 4.95-6.08‰ (n=8) and 3.53-6.58‰ (n=8). Chalcopyrite and pyrrhotite from Xinqiao have $\delta^{34}S$ values of 0.20 - 4.76‰ (n=11) and 1.92 - 5.38‰ (n=9).

307 Pyrite from the sedimentary rocks has negative $\delta^{34}S$ values. P_1q-Py, C_2c-Py, C_1g-Py and
308 D_3w-Py yielded values of -26.27 to -20.10‰ (n=6), -45.56 to -22.84‰ (n=4), -33.34 to
309 -20.44‰ (n=4) and -43.61 to -42.30‰ (n=8).
310
311 **Discussion**
312 **New insights into the origin and paragenesis of colloform pyrite**
313 A unique character of the stratabound sulfide ore deposits of the MLYB is the presence
314 of colloform pyrite, which is especially well preserved at Xinqiao. Three models have been
315 proposed for the origin of the colloform pyrite in the stratabound ore: 1) it formed by primary
316 sedimentary precipitation in the Carboniferous, based on the micro-textures and
317 nano-morphological characteristics of colloform pyrite under TEM, which have been used to
318 suggest that the nano particles of pyrite formed from bacterial activity (Xie et al. 2014; Xu et
319 al. 2020); 2) they formed in a late Carboniferous seafloor exhalative (SEDEX) system (Gu et
320 al. 2000), given that Re-Os dating of pyrite from a footwall mineralization zone beneath
321 stratabound ore yielded ages of 319 ± 13 Ma (Guo et al. 2011); 3) they formed in the
322 Cretaceous, based on Re-Os isochron ages and the isotope (S and Os) characteristics of the
323 colloform pyrite (136.6 ± 4.6Ma; Zhang et al. 2017; Li et al. 2018, 2019). The range of
324 genetic models is partly due to the lack of robust constraints on the origin and genesis of
325 colloform pyrite in stratabound ore systems.
326 It is commonly believed that the colloform pyrite ore is mainly developed far from
327 igneous rocks, and is intensively replaced by later massive euhedral coarse pyrite ore (Pan
328 and Dong 1999; Xu and Zhou 2001; Zhang et al. 2017; Li et al. 2018, 2019). No direct

329 relationship between the colloform pyrite assemblage and skarn/porphyry related minerals
330 have previously been recorded at Xinqiao. Here, we document the geological relationship
331 between colloform pyrite and skarn minerals; our results show that colloform pyrite has
332 complex relationships with Cretaceous skarn minerals (Fig. 7). For example, colloform pyrite
333 aggregates (Py1) fill the interstices between pyroxene crystals in pyroxene skarn (Figs. 7A-C),
334 indicating that the colloform pyrite crystallized later than the pyroxene. Colloform pyrite
335 assemblages also occur in hydrothermal stockworks and veins, where the colloform pyrite
336 veins are 0.5 - 2 cm wide and cut early massive pyrrhotite (Figs. 3A, 5A and 7D-F) or occur
337 as veinlets cutting magnetite ore (Figs. 7G, H). In addition, relict colloform pyrite aggregates
338 are found in the massive lead-zinc ore and are extensively replaced by coarse-grained pyrite,
339 chalcopyrite, and sphalerite (Figs. 7J-L). The paragenesis of the colloform pyrite indicates
340 that it is associated with Cretaceous skarn mineralization, and formed during the early sulfide
341 stage of the Xinqiao porphyry-skarn system (Fig. 8).

342 **The source of sulfur**

343 New SHRIMP in situ sulfur isotope data for sulfides from stratabound, skarn and
344 porphyry ore at Xinqiao and regional sedimentary rocks are presented here (Fig. 11). Previous
345 studies found no hydrothermal sulfate that crystallized during the ore-forming stage, meaning
346 that there was no fractionation of S isotopes between sulfate and sulfide at Xinqiao, and
347 consequently the S isotope ratios of the sulfides can provide insights into the ore fluid sources
348 (Ohmoto 1972; Li et al. 2017). The $\delta^{34}S$ value of fluids derived from magma at Xiqiao is
349 close to 5‰, based on the $\delta^{34}S$ values of Py6/7 from the porphyry ore (Fig. 11). The $\delta^{34}S$
350 values of pyrite from the stratabound ore at Xinqiao deposit fall in a narrow range from +3.19‰

351 to +8.58‰ (mean = +5.89‰; Fig. 11), and S isotopic compositions of chalcopyrite (mean =
352 +3.57‰) and pyrrhotite (mean = +3.84‰) show normal distribution with no significant
353 difference, suggesting that they have similar S sources. The $\delta^{34}S$ values of sulfides from the
354 stratabound ore overlap with the range of $\delta^{34}S$ from porphyry- (mean = +5.06‰) and
355 skarn-type pyrite (mean = +4.65 ‰), and also with the whole-rock sulfur isotopic
356 compositions ($\delta^{34}S$: +0.3 to +7.0 ‰; Chang et al. 1991) of Mesozoic intermediate-felsic
357 intrusions in the Tongling district. These results indicate that the colloform pyrite stockworks
358 formed from a Cretaceous magmatic S source rather a sedimentary source, given that pyrite
359 from the sedimentary rocks is characterized by strongly negative $\delta^{34}S$ values (-45.56‰ to
360 -20.10‰; Fig. 11). The narrow range of $\delta^{34}S$ of pyrites from the stratabound ore at Xinqiao
361 are markedly different from typical Devonian-Carboniferous SEDEX deposits where the
362 pyrite shows a wide range of $\delta^{34}S$ values (-40‰ to +30‰). In SEDEX systems it is generally
363 accepted that the sulfur was ultimately derived from seawater sulfate by either bacterial
364 sulfate reduction (BSR: negative $\delta^{34}S$ value) or thermochemical sulfate reduction (TSR:
365 positive $\delta^{34}S$ value) (e.g., the Carboniferous Red Dog deposit $\delta^{34}S$ value of pyrite is -45.8 to
366 +9.9‰, Kelley et al. 2004; the late Devonian Dajiangping pyrite deposit $\delta^{34}S$ value of pyrite
367 is -28.7‰ to +23.6‰, Qiu et al. 2018).

368 **The formation of colloform pyrite**

369 Formation of colloform pyrite at Xinqiao by sedimentary processes has been proposed
370 (Xie et al. 2014; Xu et al. 2020), however, we believe a sedimentary origin for the colloform
371 pyrite is unlikely because: 1) the textures observed are consistent with typical hydrothermal
372 occurrences of colloform pyrite (Figs. 5 and 7); 2) our chemical data plotted on the pyrite

373 trace element classifier of Mukherjee et al. (2017) and Gregory et al. (2019) displayed no
374 pyrite analysis that classified as sedimentary pyrite (Figs. 10A-E), and the S isotopes of the
375 colloform pyrite are also distinctly different from those of sedimentary pyrite (Fig. 11). In
376 addition, colloform pyrite is common in hydrothermal ore deposits and has been shown that
377 it can form by both supergene and hypogene processes. For example, previous studies have
378 demonstrated that colloform pyrite can occur as a secondary sulfide formed in supergene
379 profiles of VHMS deposits (Belogub et al. 2008) and in the Kotana Fe-skarn deposit (Çiftçi
380 2011). It can also form by alteration of pyrrhotite where supergene alteration is intense, and
381 it is commonly surrounded by marcasite and various Fe-oxides-hydroxides rims, or it can
382 occur as veins crosscutting pyrrhotite (Ramdohr 1980; Çiftçi 2011). Although some of the
383 colloform pyrite at Xinqiao occurs along cracks in pyrrhotite and shows textures similar to
384 supergene ore (Figs. 5A, 6A and 7E; Ramdohr 1980), but we reject supergene formation of
385 this colloform pyrite, based on this evidence: 1) SEM and Raman result indicate these
386 colloform textures consist of pyrite, not marcasite and/or Fe-oxides (Fig. 6); 2) The presence
387 of euhedral fine-grained pyrite rims at the replacement front between the colloform pyrite
388 and pyrrhotite distinguishes it from colloform pyrite in supergene ore (Fig. 6C); 3) The
389 stratabound ore has massive texture and lacks evidence for supergene leaching and related
390 secondary porosity or minerals (Figs. 3 and 7); 4) Previous studies revealed that secondary
391 sulfide minerals are characterized by light sulfur isotope compositions (−8.1 to −17.2‰;
392 Belogub et al. 2008), whereas our results show the colloform pyrite and pyrrhotite have
393 uniform positive sulfur isotope values (Fig. 11); 5) The colloform pyrite has no special
394 relationship with pyrrhotite, and it also occurs as veins cutting magnetite, or as infill around

pyroxenes, and as clusters replaced by pyrite and chalcopyrite (Fig. 7). All these features indicate the colloform pyrite at Xinqiao is hypogene.

Colloform pyrite in hypogene ore deposits generally occurs as primary sulfides that are widespread in SEDEX or VMS deposits (Barrie et al. 2009; Piercey 2015; Velasco-Acebes et al. 2019; Nozaki et al. 2021), and a few studies documented that colloform pyrite at Xinqiao has features similar to SEDEX deposits (Gu et al. 2000; Guo et al. 2011). However, the trace elements and S isotope of colloform pyrite from this study all plot outside the SEDEX fields (Figs. 10A-E and 11). Therefore, bringing together evidence from the geology, textures and geochemistry (trace elements and S isotopes) of the colloform pyrite, we propose that the colloform pyrite at Xinqiao is a product of the skarn ore system.

Previous studies proposed that colloform pyrite and corresponding trace element enrichment (i.e., As, Au, Mo, Tl, etc.) are common in porphyry-related epithermal environments, and suggest it probably resulted from rapid disequilibrium precipitation and high growth rates in a relatively low temperature environment (Fleet et al. 1989; Huston et al. 1995; Peterson and Mavrogenes 2014; Franchini 2015; Sykora et al. 2018). We infer that the colloform textures and chalcophile element enrichment in pyrite from the stratabound ore at Xinqiao is consistent with rapid disequilibrium precipitation. This rapid precipitation is supported by the abundant micron- or nanometer-sized (200nm to 2 μm) cubic pyrite {100+111} aggregates that form the colloform texture observed in this study (Fig. 6) and previous papers (Xie et al. 2014; Zhang et al. 2017; Li et al. 2018). In addition, fluid inclusions in quartz from colloform pyrite ore indicate that it formed at around 200~300°C (Li et al. 2017), consistent with previous experiments that indicated that the pyrite cubes with

417 smooth α{100} faces and small o{111} formed at 250°C and moderately supersaturated
418 conditions (Murowchick and Barnes 1987). Abraitis et al. (2004) further suggested that fast
419 crystallization helps incorporate trace elements by adsorption into pyrite, as at slower rates Fe
420 and S atoms are likely to displace other ions and form more thermodynamically stable cubic
421 pyrite. Notably, the supersaturated crystallization of pyrite at Xinqiao was mainly caused by
422 abrupt change in physic-chemical conditions of the ore-bearing hydrothermal fluid when the
423 magmatic-hydrothermal fluid (derived from Cretaceous magma) flowed along the
424 Devonian-Carboniferous unconformity.

425 **Systematic geochemical variations of pyrite and their implications**

426 Our point and element mapping geochemical data show that the greatest trace element
427 variation of pyrites from stratabound, skarn, and porphyry ore are in Co, Ni, Se, As, Cu, Pb,
428 Zn, Ag, and Bi (Figs. 9 and 10). LA-ICP-MS time-resolved signal spectra and mapping
429 indicate these elements are homogeneously distributed in the lattice of most analyzed pyrites,
430 whereas Pb-bearing inclusions (probably galena) are common in Py2/4/5 and Pb-Bi-Ag-Te
431 bearing sub-microscopic inclusions also occurs in a few Py4 grains (Fig. 12). These
432 differences in trace element compositions in pyrite can be controlled by fluid composition,
433 fluid conditions, kinetic processes and the co-precipitating minerals (Large et al. 2009; Sykora
434 et al. 2018).

435 A significant decrease in Co, Ni, and Se is observed from Py7/6 to Py1 at Xinqiao, with
436 the contents of Co, Ni, and Se in Py7/6 from the porphyry ore being two orders of magnitude
437 higher than in Py1 from the stratabound ore (Figs. 10A, F). The enrichment of Co, Ni and Se
438 in pyrite from the porphyry mineralization zone is consistent with pyrite formed at high

439 temperature in a porphyry environment (e.g., Dexing deposit, Reich et al. 2013; Lihir deposit,
440 Sykora et al. 2018), based on observations that Co, Ni, and Se tend to be more efficiently
441 incorporated into pyrite under high temperature conditions (Hanley and MacKenzie 2009;
442 Gregory et al. 2013; Reich et al. 2013; Sykora et al. 2018). The K-feldspar and actinolite
443 selvages to the quartz-pyrite veins also indicate that the fluid responsible for the potassic
444 mineralization was relatively high temperature (Xiao et al. 2021). However, most metallic
445 elements (e.g., Cu, Pb, Zn and Ag) are depleted in Py7/6 (Fig. 10G), possibly due to the fluid
446 conditions and the nature of the co-precipitating minerals, because Cu was mainly deposited
447 as chalcopyrite in the porphyry-type mineralization zone, and Pb, Zn, Ag remained in solution
448 in the high T magmatic-hydrothermal fluid (Kouzmanov and pokrovski 2012). In addition,
449 NaOCl etching and trace element LA-ICP-MS images revealed strong oscillatory zones in
450 Py7 grains (Fig. 9C); the inhomogeneous oscillatory distribution of Co, Ni and Se may
451 indicate local episodic fluctuations in fluid composition. Most trace elements in Py5 from the
452 massive skarn-type pyrite-chalcopyrite ore have low concentrations, typically less than 10
453 ppm (Fig. 10), which may have resulted from precipitation of large amounts of sulfide
454 (pyrite-chalcopyrite) in the porphyry ore and coexistence of chalcopyrite in skarn ore.
455 However, Py4/4a from distal skarn ore has higher concentrations of Zn, Cu, Pb, Bi and Ag,
456 whereas they are depleted in Co, Ni, and Se compared to pyrite from the porphyry and
457 proximal skarn ore (Fig. 10). Previous studies have interpreted this change as resulting from
458 decreasing ore-forming fluid temperature (Fleet et al. 1989; Reich et al. 2013; Sykora et al.
459 2018; Keith et al. 2018; Steadman et al. 2020). At the same time, increasing fluid pH where
460 intense fluid-rock reaction occurred in distal skarn may have also contributed to Zn

461 enrichment in Py4 (Fig. 10B); thermodynamic data indicate pH increase aids Zn precipitation
462 from both high and low temperature fluids (Kouzmanov and Pokrovski 2012; Zhang et al.
463 2022).

464 Three pyrite types from the stratabound ore display differences in trace element contents
465 (Figs. 9 and 10). Colloform pyrite (Py1) is enriched in most chalcophile elements (Cu, Pb, Zn,
466 Ag, Bi, Sb, As and Tl, Fig. 10), but depleted in Co, Ni and Se (all less than 10 ppm). It has
467 trace element concentrations similar to pyrite from the distal marble zone, suggesting that
468 they may have formed in the same fluid environment (Fig. 10), and further supporting a
469 magmatic-hydrothermal origin as the metallic elements were probably derived from magmas
470 (Li et al. 2018). In addition, the sharp contact relationship between Py1 and Py2, and the fact
471 that both are cut by Py3, indicate they formed from multi-stage hydrothermal fluids (Fig. 5).
472 Py2 is enriched in As and Py3 has high Co and Ni contents compared to Py1 (Figs. 9 and 10);
473 the changes of trace elements suggest they formed from fluids with different compositions
474 and/or physicochemical conditions (Large et al. 2009; Smith et al. 2014). Py3 shows
475 geochemistry (Co, Ni and Se) similar to pyrite from the porphyry ore, suggesting it may have
476 crystallized from a later stage high-T hydrothermal fluid, as Co, Ni and Se are strongly
477 associated with high-T environments in porphyry systems (Hanley and MacKenzie, 2009;
478 Gregory et al., 2013; Reich et al., 2013). These compositional variations in different stages of
479 pyrite are compelling evidence for multi-stage mineralization of the stratabound ore at
480 Xinqiao.

481 **The formation of stratabound ore and implications**

482 The geological (textures and paragenesis) and chemical (trace elements and S isotope)

This is the peer-reviewed, final accepted version for American Mineralogist, published by the Mineralogical Society of America.
The published version is subject to change. Cite as Authors (Year) Title. American Mineralogist, in press.
DOI: https://doi.org/10.2138/am-2022-8527. http://www.minsocam.org/

483 evidence indicate that the stratabound ore in the Tongling district has a Cretaceous magmatic
484 origin formed during multiple mineralization stages (Figs. 13A-C). The first stage formed
485 distal colloform-texture pyrite ore (Fig. 13C), which aggregated from abundant
486 nanometer-scale pyrite cubes (Fig. 6). The pyrite cubes probably formed by rapid nucleation
487 from a high fS_2 and low temperature supersaturated solution (Murowchick and Barnes 1987;
488 Butler and Rickard 2000; Abraitis et al. 2004) that probably formed by two processes: 1)
489 rapid decompression of magmatic-hydrothermal fluids derived from the Cretaceous intrusions,
490 flowing along the unconformity between the Devonian and the Carboniferous; 2) intensive
491 water-rock interaction between early Cretaceous magmatic-hydrothermal fluids and
492 Carboniferous-Permian reduced wall rocks, which promoted reduction of the sulfur.
493 Water-rock interaction at Xinqiao was proved by the highly radiogenic Os_i value of colloform
494 pyrite reported by Li et al. 2018. Later addition of magmatic-hydrothermal fluids formed the
495 massive coarse-grained pyrite (Py2) that replaced/overprinted the early colloform pyrite (Py1)
496 ore, and ultimately formed the chalcopyrite-pyrite (Py3)-quartz veins that cut Py1 and Py2
497 (Fig. 13B). These multi-stage pyrite + chalcopyrite veins comprise the most economically
498 important part of the stratabound ore (Fig. 13).

499 **Pyrite chemistry indicators of mineralization styles and exploration in porphyry Cu**
500 **systems**

501 Stratabound ore has been recognized as an end member in some porphyry copper
502 systems (Sillitoe 2010) and is well documented in north-central Chile (Reyes 1991).
503 Stratabound Cu deposits similar to the one at Xinqiao are widespread in the MLYB, and show
504 affinities to the early Cretaceous porphyry-skarn Cu systems that cluster in the Tongling and

505 Jiurui districts (Fig.1; Pan and Dong 1999; Mao et al. 2009). Pyrite is the main sulfide mineral
506 in stratabound, skarn and porphyry ores, and shows varied textures and chemistry that can be
507 used to identify different ore types in the porphyry Cu systems, based on our data and
508 previously published data from stratabound, skarn, and porphyry ore from several deposits in
509 the MLYB (Tongling district:Taoyuan, Xinqiao, Dongguashan, Shujiadian, Fenghuangshan;
510 Jiurui district: Chengmenshan and Jinjiwo).

511 Overall, pyrite from skarn ore and porphyry ore show similar geochemical character,
512 with higher concentration of Co and Ni than stratabound ore, whereas As, Sb, Pb, Bi, and Ag
513 are relatively enriched in pyrite from stratabound ore (Fig. 14). As discussed above,
514 temperature exerts a first-order control on the trace elements trend in pyrite from stratabound,
515 skarn and porphyry ore; the lowering of fluid temperature from porphyry/skarn ore to
516 stratabound ore has been demonstrated by fluid inclusion data in previous studies (Li et al.
517 2017). We use a plot of As/Se versus Co to discriminate the three ore types (Fig. 14C), as
518 these elements are abundant, they are sensitive to fluid condition (especially T; Migdisov et al.
519 2011; Deditius et al. 2014), and they mainly occur in the pyrite crystal lattice, rather than in
520 mineral inclusions. In addition, Herazo et al. (2021) showed that pyrite in volcanic-hosted
521 stratabound ore deposits in northern Chile has significant levels of Cu, As, Mn, Pb, Tl, Co, Ni,
522 V, and Mo, with high Ag/Co and low Co/Cu and Co-Ni ratios compared to high-T iron
523 oxide-apatite and iron oxide copper-gold systems.

524 Cobalt, Ni, and Se are higher in porphyry- and skarn- type pyrite in deposits in the
525 MLYB, and stratabound ore has the highest As/Se ratio and low Co values, making them
526 readily distinguished from skarn and porphyry ore; in addition, stratabound ore commonly

527 extends for 1-2 km away from the intrusion, suggesting potential to use trace elements such as
528 As, Sb, Pb, Bi, and Ag in pyrite as distal pathfinder elements during exploration in the MLYB
529 and elsewhere.

530 **Conclusion and Implication**

531 Colloform pyrite has been commonly considered to form as a result of seafloor
532 exhalative sedimentary processes, and reports claim it is rare in porphyry-skarn systems.
533 Colloform pyrite is abundant in the stratabound ore of the Middle-Lower Yangtze River
534 metallogenic belt, eastern China. Based on the typical hydrothermal stockwork occurrence of
535 colloform pyrite and its geochemical signatures (trace elements and S isotopes) at Xinqiao we
536 propose the colloform pyrite is related to Cretaceous porphyry-skarn mineralization, rather
537 than Carboniferous syn-sedimentary or seafloor sedimentary exhalative processes. We suggest
538 that Co, Ni, and Se substituted into porphyry- and skarn-type pyrite at high temperature,
539 whereas the As, Cu, Pb, Zn, Ag and Bi were incorporated into colloform pyrite during rapid
540 crystallization. This study shows that colloform pyrite can occur in porphyry-skarn ore
541 systems, and various features of the pyrites can effectively fingerprint the stratabound
542 mineralization and show that it formed from multiple influxes of magmatic-hydrothermal
543 fluids derived from an Early Cretaceous stock. Furthermore, pyrite trace elements are shown
544 to be useful indicators of mineralization type in porphyry-skarn Cu systems, with Co and Ni
545 increasing towards porphyry and skarn ore, whereas As, Sb, Pb, Ag and Bi are enriched in
546 pyrite from distal stratabound ore. These results indicate pyrite chemistry can as an effective
547 indicator of deposit type and provides potential vectors for exploration in porphyry-skarn
548 systems in the MLYB and elsewhere.

Acknowledgments

We thank Yixia Wang at the Xinqiao mine for help with sampling, and Sebastien Meffre, Sandrin Feig, Karsten Goemann, Jay Thompson and Paul Olin at CODES and the Central Science Laboratory (CSL), University of Tasmania, for their help with samples and analyses. This work was financially supported by the National Natural Science Foundation of China (grants 91962218, 41320104003).

References

803-Geological-Team. (1971) Reserves Report of Xinqiao Cu Bearing Pyrite Deposits, Tonglong, Anhui. Metallurgical Geology Bureau of Anhui Province, p. 141 (in Chinese).

Abraitis, P.K., Pattrick, R.A.D., and Vaughan, D.J. (2004). Variations in the compositional, textural and electrical properties of natural pyrite: a review. International Journal of Mineral Processing, 74(1-4), 41-59.

Barrie, C.D., Boyce, A.J., Boyle, A.P., Williams, P.J., Blake, K., Ogawara, T., Akai, J., and Prior, D.J. (2009) Growth controls in colloform pyrite. American Mineralogist, 94(4), 415-429.

Belogub, E.V., Novoselov, K.A., Yakovleva, V.A., and Spiro, B. (2008) Supergene sulphides and related minerals in the supergene profiles of VHMS deposits from the South Urals. Ore geology reviews, 33(3-4), 239-254.

Butler, I.B., and Rickard, D. (2000). Framboidal pyrite formation via the oxidation of iron (II) monosulfide by hydrogen sulphide. Geochimica et Cosmochimica Acta, 64(15), 2665-2672.

571 Chang, Y.F., Liu, X.P., and Wu, Y.Z. (1991) Metallogenic belt of the Middle-Lower Yangtze
572 River. Beijing: Geological Publishing House, 1–379 (in Chinese).
573 Ciftci, E. (2011) Sphalerite associated with pyrrhotite-chalcopyrite ore occurring in the
574 Kotana Fe-skarn deposit (Giresun, NE Turkey): exsolution or replacement. Turkish
575 Journal of Earth Sciences, 20(3), 307-320.
576 Crowe, D.E., and Vaughan, R.G. (1996) Characterization and use of isotopically
577 homogeneous standards for in situ laser microprobe analysis of $^{34}S/^{32}S$ ratios. American
578 Mineralogist, 81(1-2), 187-193.
579 Danyushevsky, L., Robinson, P., Gilbert, S., Norman, M., Large, R., McGoldrick, P., and
580 Shelley, M. (2011) Routine quantitative multi-element analysis of sulphide minerals by
581 laser ablation ICP-MS: Standard development and consideration of matrix effects.
582 Geochemistry: Exploration, Environment, Analysis, 11(1), 51-60.
583 Deditius, A., Utsunomiya, S., Reich, M., Kesler, S., Ewing, R., Hough, R., and Walshe, J.
584 (2011) Trace metal nanoparticles in pyrite. Ore Geology Reviews, 42, 32–46.
585 Du, H., Zheng, J., Tian, L., Liang, H., Guo, J., and Li, Y. (2020) Microfabrics, in-situ trace
586 element and sulfur isotope compositions of pyrite from the Jinjiwo copper deposit in
587 Chengmenshan orefield, northern Yangtze Block: Syngenetic stratabound mineralization
588 and hydrothermal remobilization. Ore Geology Reviews, 127, 103830.
589 Fleet, M.E., MacLean, PJ., and Barbier, J. (1989) Oscillatory-zoned As-bearing pyrite from
590 strata-bound and stratiform gold deposits: An indicator of ore fluid evolution. Economic
591 Geology Monograph 6, 356-362.
592 Fontboté, L., and Gorzawski, H. (1990) Genesis of the Mississippi Valley-type Zn-Pb deposit

593 of San Vicente, central Peru; geologic and isotopic (Sr, O, C, S, Pb) evidence. Economic
594 Geology, 85(7), 1402-1437.
595 Franchini, M., McFarlane, C., Maydagán, L., Reich, M., Lentz, D. R., Meinert, L., and
596 Bouhier, V. (2015) Trace metals in pyrite and marcasite from the Agua Rica
597 porphyry-high sulfidation epithermal deposit, Catamarca, Argentina: Textural features
598 and metal zoning at the porphyry to epithermal transition. Ore Geology Reviews, 66,
599 366-387.
600 Gregory, D.D., Cracknell, M.J., Large, R.R., McGoldrick, P., Kuhn, S., Maslennikov, V.V.,
601 Baker, M.J., Fox, N., Belousov, I., and Figueroa, M. C. (2019) Distinguishing Ore
602 Deposit Type and Barren Sedimentary Pyrite Using Laser Ablation-Inductively Coupled
603 Plasma-Mass Spectrometry Trace Element Data and Statistical Analysis of Large Data
604 Sets. Economic Geology, 114(4), 771- 786.
605 Gregory, D.D., Large, R.R., Bath, A.B., Steadman, J.A., Wu, S., Danyushevsky, L., Bull, S.
606 W., Holden, P., and Ireland, T.R. (2016) Trace Element Content of Pyrite from the Kapai
607 Slate, St. Ives Gold District, Western Australia: Economic Geology, 111(6), 1297-1320.
608 Gregory, M.J., Lang, J.R., Gilbert, S., and Hoal, K.O. (2013) Geometallurgy of the Pebble
609 porphyry copper-gold-molybdenum deposit, Alaska: Implications for gold distribution
610 and paragenesis. Economic Geology, 108(3), 463-482.
611 Gu, L.X., Hu,W.X., He, J.X., Ni, P., Xu, K.Q. (2000) Regional variations in ore composition
612 and fluid features of massive sulphide deposits in South China: implications for genetic
613 modelling. Episodes 23, 110–118.
614 Gu, L.X., Zaw, K., Hu, W.X., Zhang, K.J., Ni, P., He, J.X., Xu, Y.T., Lu, J.J., Lin, C.M. (2007)

615 Distinctive features of Late Palaeozoic massive sulphide deposits in South China. Ore
616 Geology Reviews, 31(1-4), 107-138.
617 Guo, W.M., Lu, J.J., Jiang, S.Y., Zhang, R.Q., Qi, L. (2011) Re-Os isotope dating of pyrite
618 from the footwall mineralization zone of the Xinqiao deposit, Tongling, Anhui Province:
619 geochronological evidence for submarine exhalative sedimentation. Chinese Science
620 Bulletin, 56(35), 3860-3865 (in Chinese).
621 Han (2020) Geology and mineralization of the Cu-Au skarn system in southeast Hubei
622 Province and northwest Jiangxi Province, eastern China: Examples from the Fengshang
623 and Chengmenshan areas in Jiurui ore district. Doctoral dissertation, China University of
624 Geosciences (in Chinese).
625 Hanley, J.J., and MacKenzie, M.K. (2009) Incorporation of platinum-group elements and
626 cobalt into subsidiary pyrite in alkalic Cu-Au porphyry deposits: significant implications
627 for precious metal distribution in felsic magmatic-hydrothermal systems. In AGU Spring
628 Meeting Abstracts (Vol. 2009, pp. V14A-03).
629 Herazo, A., Reich, M., Barra, F., Morata, D., and Real, I.D. (2021) Trace element
630 geochemistry of pyrite from bitumen-bearing stratabound Cu–(Ag) deposits, Northern
631 Chile. ACS Earth and Space Chemistry, 5(3), 566-579.
632 Huston, D.L., Sie, S.H., Suter, G.F., Cooke, D.R., and Both, R.A. (1995) Trace elements in
633 sulfide minerals from eastern Australian volcanic-hosted massive sulfide deposits; Part I,
634 Proton microprobe analyses of pyrite, chalcopyrite, and sphalerite, and Part II, Selenium
635 levels in pyrite; comparison with delta ^{34} S values and implications for the source of
636 sulfur in volcanogenic hydrothermal systems. Economic Geology, 90(5), 1167-1196.

637 Ireland, T.R., Clement, S., Compston, W., Foster, J.J., Holden, P., Jenkins, B., lanc, P., Schram,
638 N., and Williams, I.S. (2008) Development of SHRIMP. Australian Journal of Earth
639 Sciences, 55(6-7), 937-954.
640 Ireland, T.R., Schram, N., Holden, P., Lanc, P., Ávila, J., Armstrong, R., Amelin,Y., Latimore,
641 A., Corrigan, D., Clement, S., Foster, J.J., and Compston, W. (2014) Charge-mode
642 electrometer measurements of S-isotopic compositions on SHRIMP-SI. International
643 Journal of Mass Spectrometry, 359, 26-37.
644 Jochum, K.P., Pfänder, J., Woodhead, J.D., Willbold, M., Stoll, B., Herwig, K., Amini, M.,
645 Abouchami, W., and Hofmann, A.W. (2005) MPI-DING glasses: New geological
646 reference materials for in situ Pb isotope analysis. Geochemistry, Geophysics,
647 Geosystems, 6, 1525–2027.
648 Keith, M., Smith, D.J., Jenkin, G.R., Holwell, D.A., and Dye, M.D. (2018) A review of Te and
649 Se systematics in hydrothermal pyrite from precious metal deposits: Insights into
650 ore-forming processes. Ore Geology Reviews, 96, 269-282.
651 Kelley, K.D., Leach, D.L., Johnson, C.A., Clark, J.L., Fayek, M., Slack, J.F., Anderson, V,M.,
652 Ayuso, R.A., and Ridley, W.I. (2004) Textural, compositional, and sulfur isotope
653 variations of sulfide minerals in the Red Dog Zn-Pb-Ag deposits, Brooks Range, Alaska:
654 Implications for ore formation. Economic Geology, 99(7), 1509-1532.
655 Kouzmanov, K., and Pokrovski, G.S. (2012) Hydrothermal controls on metal distribution in
656 porphyry Cu (-Mo-Au) systems. Special publications of the Society of Economic
657 Geologists, 16, 573-618.
658 Large, R.R., Danyushevsky, L., Hollit, C., Maslennikov, V., Meffre, S., Gilbert, S., Bull, S.,

659 Scott, R., Emsbo, P., Thomas, H., Singh, B., and Foster, J. (2009) Gold and trace element
660 zonation in pyrite using a laser imaging technique: implications for the timing of gold in
661 orogenic and Carlin-style sediment-hosted deposits. Economic Geology, 104(5),
662 635-668.
663 Laznicka, P. (1981). A computerized research file on global metallogeny—An experience
664 with MANIFILE. Global Tectonics and Metallogeny, 224-245.
665 Li, Y., Li, J.W., Li, X.H., Selby, D., Huang, G.H., Chen, L.J., and Zheng, K. (2017) An Early
666 Cretaceous carbonate replacement origin for the Xinqiao stratabound massive sulfide
667 deposit, Middle-Lower Yangtze metallogenic belt, China. Ore Geology Reviews, 80,
668 985-1003.
669 Li, Y., Li, Q.L., and Yang, J.H. (2019). Tracing water-rock interaction in carbonate
670 replacement deposits: a SIMS pyrite S-Pb isotope perspective from the Chinese Xinqiao
671 system. Ore Geology Reviews, 107, 248-257.
672 Li, Y., Selby, D., Li, X.H., and Ottley, C.J. (2018) Multisourced metals enriched by
673 magmatic-hydrothermal fluids in stratabound deposits of the Middle–Lower Yangtze
674 River metallogenic belt, China. Geology, 46(5), 391-394.
675 Mao, J.W., Xie, G.Q., Duan, C., Pirajno, F., Ishiyama, D., Chen, Y.C. (2011) A
676 tectono-genetic model for porphyry-skarn-stratabound Cu-Au-Mo-Fe and
677 magnetite-apatite deposits along the middle-lower Yangtze River Valley, Eastern China.
678 Ore Geology Reviews, 43, 294–314.
679 Mao, J.W., Zhou, T.F., Xie, G.Q., Yuan, F., and Duan, C. (2020) Metallogeny in
680 Middle-Lower Yangtze River Ore Belt: Advances and problems remained. Mineral

681 Deposits, 39(4), 547-558 (In Chinese).

682 Meinert, L.D. (1982) Skarn, manto, and breccia pipe formation in sedimentary-rocks of the
683 Cananea Mining District, Sonora, Mexico. Economic Geology, 77, 919-949.

684 Migdisov, A.A., Zezin, D., and Williams-Jones, A.E. (2011) An experimental study of cobalt
685 (II) complexation in Cl– and H2S-bearing hydrothermal solutions. Geochimica et
686 Cosmochimica Acta, 75, 4065–4079.

687 Mukherjee, I., and Large, R. (2017) Application of pyrite trace element chemistry to
688 exploration for SEDEX style Zn-Pb deposits: McArthur Basin, Northern Territory,
689 Australia. Ore Geology Reviews, 81, 1249-1270.

690 Murowchick, J.B., and Barnes, H.L. (1987) Effects of temperature and degree of
691 supersaturation on pyrite morphology. American Mineralogist, 72(11-12), 1241-1250.

692 Nozaki, T., Nagase, T., Ushikubo, T., Shimizu, K., and Ishibashi, J.I. (2021) Microbial sulfate
693 reduction plays an important role at the initial stage of subseafloor sulfide mineralization.
694 Geology, 49(2), 222-227.

695 Ohmoto, H. (1972) Systematics of sulfur and carbon isotopes in hydrothermal ore deposits.
696 Economic Geology, 67(5), 551-578.

697 Pan, Y.M., and Dong, P. (1999) The Lower Changjiang (Yangzi/Yangtze River) metallogenic
698 belt, east central China: intrusion-and wall rock-hosted Cu–Fe–Au, Mo, Zn, Pb, Ag
699 deposits. Ore Geology Reviews, 15(4), 177-242.

700 Peterson, E.C., and Mavrogenes, J.A. (2014) Linking high-grade gold mineralization to
701 earthquake-induced fault-valve processes in the Porgera gold deposit, Papua New
702 Guinea. Geology, 42(5), 383-386.

703 Philippot, P., Ávila, J.N., Killingsworth, B.A., Tessalina, S., Baton, F., Caquineau, T., Muller,
704 E., Pecoits, E., Cartigny, P., Lalonde, S.V., Ireland, T.R., Thomazo, C., Kranendonk, M.J.,
705 and Busigny, V. (2018) Globally asynchronous sulphur isotope signals require
706 re-definition of the Great Oxidation Event. Nature communications, 9(1), 1-10.
707 Piercey, S.J. (2015) A semipermeable interface model for the genesis of subseafloor
708 replacement-type volcanogenic massive sulfide (VMS) deposits. Economic Geology,
709 110(7), 1655-1660.
710 Qiu, W.J., Zhou, M.F., Li, X., Williams-Jones, A.E., and Yuan, H. (2018) The genesis of the
711 giant Dajiangping SEDEX-type pyrite deposit, South China. Economic Geology, 113(6),
712 1419-1446.
713 Ramdohr, P. (1980) The Ore Minerals and their Intergrowths, 2nd ed. Pergamon Press, New
714 York, 1207 p.
715 Reich, M., Deditius, A., Chryssoulis, S., Li, J.W., Ma, C.Q., Parada, M.A., Barra, F., and
716 Mittermayr, F. (2013) Pyrite as a record of hydrothermal fluid evolution in a porphyry
717 copper system: A SIMS/EMPA trace element study. Geochimica et Cosmochimica Acta,
718 104, 42-62.
719 Reyes, M. (1991) The Andacollo strata-bound gold deposit, Chile, and its position in a
720 porphyry copper-gold system. Economic Geology, 86(6), 1301-1316.
721 Sillitoe, R.H. (2010) Porphyry copper systems. Economic Geology, 105, 3–41.
722 Smith, J.W., Holwell, D.A., McDonald, I. (2014) Precious and base metal geochemistry and
723 mineralogy of the Grasvally Norite-Pyroxenite Anorthosite (GNPA) member, northern
724 Bushveld Complex, South Africa: implications for a multistage emplacement.

Mineralium Deposita, 49(6), 667-692.

Steadman, J.A., Large, R.R., Olin, P.H., Danyushevsky, L.V., Meffre, S., Huston, D., Fabris, A., Lisitsin, V., and Wells, T. (2021) Pyrite trace element behavior in magmatic-hydrothermal environments: An LA-ICPMS imaging study. Ore Geology Reviews, 128, 103878.

Sykora, S., Cooke, D.R., Meffre, S., Stephanov, A.S., Gardner, K., Scott, R., Selley, D., and Harris, A.C. (2018) Evolution of pyrite trace element compositions from porphyry-style and epithermal conditions at the Lihir gold deposit: Implications for ore genesis and mineral processing. Economic Geology, 113(1), 193-208.

Tang, Y.C., Wu, Y.Z., Cu, G.Z., Xing, F.M., Wang, Y.M., Cao, F.Y., and Chang, Y.F. (1998) Copper gold polymetallic ore deposit geology in the region along Yangtze River in Anhui Province. Beijing: Geological Publishing House, 1–351 (in Chinese).

Tanner, D., Henley, R.W., Mavrogenes, J.A., and Holden, P. (2016) Sulfur isotope and trace element systematics of zoned pyrite crystals from the El Indio Au–Cu–Ag deposit, Chile. Contributions to Mineralogy and Petrology, 171(4), 1-17.

Velasco-Acebes, J., Tornos, F., Kidane, A.T., Wiedenbeck, M., Velasco, F., and Delgado, A. (2019) Isotope geochemistry tracks the maturation of submarine massive sulfide mounds (Iberian Pyrite Belt). Mineralium Deposita, 54(6), 913-934.

Wang, S.W., (2015) Porphyry deposits and associated magmatic activity in the Anhui segment of the Middle Lower Yangtze River Valley metallogenic belt. Doctoral dissertation, Hefei University of Technology (in Chinese).

Wang, Y.B., Liu, D.Y., Meng, Y.F., Zeng, P.S., Yang, Z.S., and Tian, S.H. (2004) SHRIMP

U-Pb geochronology of the Xinqiao Cu-S-Fe-Au deposit in the Tongling ore district, Anhui. Geology in China, 31, 169–173 (In Chinese with English Abstract).

Xiao, X., Zhou, T.F., White, N.C., Zhang, L.J., Fan, Y., Wang, F.Y., and Chen, X.F. (2018) The formation and trace elements of garnet in the skarn zone from the Xinqiao Cu-S-Fe-Au deposit, Tongling ore district, Anhui Province, Eastern China. Lithos, 302, 467-479.

Xiao, X., Zhou, T.F., White, N.C., Zhang, L.J., Fan, Y., Wang, F.Y., and Chen, X.F. (2021) Porphyry Cu mineralization processes of Xinqiao deposit, Tongling ore district: Constraints from the geochronology and geochemistry of zircon, apatite, and rutile. Ore Geology Reviews, 138, 104340.

Xie, J.C., Ge, L.K., Fang, D., Li, Q.Z., Qian, L., Li, Z.S., Yan, J and Sun, W.D., (2020b) Geochemistry of pyrite from stratabound massive sulfide deposits, Tongling region, China: Implication for their genesis. Ore Geology Reviews, 120, 103430.

Xie, J.C., Ge, L.K., Qian, L., Li, Q.Z., and Sun, W.D (2020a). Trace element characteristics of pyrite in Dongguashan Cu (Au) deposit, Tongling region, China. Solid Earth Sciences, 5(4), 233-246.

Xie, Q.Q., Chen, T.H., Fan, Z.L., Xu, X.C., Zhou,Y.F., Shi, W.B., and Xue, J.J. (2014) Morphological characteristics and genesis of colloform pyrite in Xinqiao Fe-S deposit, Tongling, Anhui Province: Scientia Sinica Terrae, v. 44, p. 2665-2674 (in Chinese).

Xu, G., and Zhou, J., 2001. The Xinqiao Cu-S-Fe-Au deposit in the Tongling mineral district, China: synorogenic remobilization of a stratiform sulfide deposit. Ore Geology Reviews, 18(1-2), 77-94.

Xu, L., Xie, Q., Chen, T.H., Xu, X.C., Zhou, Y.F., Sun, S.H., and Chen, P. (2020) Genesis of Strata-bound Sulfide Orebodies in the Tongling Polymetallic Mineralization Cluster, SE China: Evidence from Colloform Pyrite. Acta Geologica Sinica (English Edition), 94(6), 1849-1859.

Zhang, Y., Chen, H.Y., Cheng, J.M., Tian, J., Zhang, L.J., and Olin P. (2022) Pyrite geochemistry and its implications on Au-Cu skarn metallogeny: An example from the Jiguanzui deposit, Eastern China. American Mineralogist (in press). DOI: https://doi.org/10.2138/am-2022-8118.

Zhang, Y., Hollings, P., Shao, Y.J., Li, D.F., Chen, H.Y., and Li, H.B. (2020) Magnetite texture and trace-element geochemistry fingerprint of pulsed mineralization in the Xinqiao Cu-Fe-Au deposit, Eastern China. American Mineralogist: Journal of Earth and Planetary Materials, 105(11), 1712-1723.

Zhang, Y., Shao, Y.J., Chen, H.Y., Liu, Z.F., and Li, D.F. (2017) A hydrothermal origin for the large Xinqiao Cu-S-Fe deposit, Eastern China: Evidence from sulfide geochemistry and sulfur isotopes. Ore Geology Reviews, 88, 534-549.

Zhou, T.F., Wang, S.W., Fan, Y., Yuan, F., Zhang, D.Y., and White, N.C. (2015) A review of the intracontinental porphyry deposits in the Middle-Lower Yangtze River Valley metallogenic belt, Eastern China. Ore Geology Reviews, 65, 433-456.

Zhou, T.F., Zhang, L.J., Yuan, F., Fan, Y. (2010) LA-ICP-MS in situ trace element analysis of pyrite from the Xinqiao C-Au-S deposit in Tongling, Anhui, and its constraints on the ore genesis. Earth Science Frontiers, 17, 306–319 (In Chinese with English Abstract).

791 **Figure Captions**

792 **Figure 1.** (A) Location of the Middle–Lower Yangtze River metallogenic belt; (B) Geological
793 map of magmatic rocks and deposits in the Middle-Lower Yangtze River Valley metallogenic
794 belt (modified after Pan and Dong 1999); (C) Geological map of Tongling district, Anhui,
795 eastern China (modified after Chang et al. 1991). TLF: Tancheng-Lujiang fault; XGF:
796 Xiangfan-Guangji fault; HPF: Huanglishu-Poliangting fault; CHF: Chuhe fault; CCF:
797 Chongyang-Changzhou fault; JNF: Jiangnan fault

798

799 **Figure 2.** (A) Geological sketch map of the Xinqiao ore deposit (after Tang et al. 1998); (B)
800 Representative cross sections of Xinqiao deposit (after 803-Geological-Team 1971).

801

802 **Figure 3.** Representative examples of pyrite in stratabound, skarn and porphyry ore in
803 Xinqiao deposit. (A) Stratabound ore consist of massive dark-grey colloform pyrite ore
804 replacing massive pyrrhotite and (B) massive pyrite-quartz (chalcopyrite) ore; (C) distal skarn
805 ore (magnetite and pyrite in marble); (D) massive pyrite-chalcopyrite skarn ore; (E)
806 quartz-pyrite-hematite (chalcopyrite) vein with muscovite halos in the phyllic alteration zone;
807 (F) quartz-pyrite-chalcopyrite vein with K-feldspar halos in potassic alteration zone.

808

809 **Figure 4.** The petrology of sedimentary pyrite in regional sedimentary rocks. (A) Permian
810 Qixia Formation (P_1q) limestone; (B) Disseminated fine-grained subhedral pyrite in Qixia
811 limestone; (C) Carboniferous Chuanshan-Huanglong Formation (C_2c); (D) Fine-grained

812 anhedral pyrite cluster in Chuanshan-Huanglong limestone; (E) Carboniferous Gaolishan
813 Formation (C_1g); (F) Fine-grained oolitic pyrite cluster in Gaolishan silty shale; (G) Upper
814 Devonian Wutong Formation (D_3w); (H) Coarse-grained euhedral pyrite in Wutong
815 sandstone.
816
817 **Figure 5.** Microscopic characteristics and types of pyrite in stratabound (Py1, 2 and 3), skarn
818 (Py4a, 4 and 5) and porphyry ore (Py6 and 7) from the Xinqiao deposit. (A) Py1 (colloform
819 pyrite) occurs as stockwork replacing pyrrhotite; (B-E) Py1 replaced by coarse-grained
820 anhedral pyrite (Py2) and fine-grained pyrite (Py3)-chalcopyrite-vein; (F) Subhedral coarse
821 pyrite (Py4) and fine-grained pyrite vein (Py4a) in pyrite vein from distal skarn ore; (G)
822 Subhedral coarse pyrite (Py5) in massive pyrite-chalcopyrite ore; (H) Subhedral coarse pyrite
823 (Py6) in phyllic alteration zone; (I) NaOCl etched subhedral coarse pyrite (Py7) in potassic
824 alteration zone showing oscillatory zones.
825
826 **Figure 6.** The Raman spectra, BSE and SEM images of colloform pyrite from Xinqiao. (A)
827 Colloform pyrite occurs as vein cutting pyrrhotite and showing obvious zoning; (B) Raman
828 spectra of colloform pyrite bands; (C) BSE image showing colloform pyrite has a sharp
829 contact with pyrrhotite and micro euhedral pyrite present in replacement front; (D, E) SEM
830 images showing colloform pyrite consists of nanometer-scale pyrite cubes.
831
832 **Figure 7.** Photomicrographs showing petrological features of colloform pyrite and its
833 relationship with oxide and sulfide assemblages in Xinqiao deposits. (A) Colloform pyrite

834 (Py1) with chalcopyrite replacing pyroxene skarn; (B-C) Colloform pyrite (Py1) infilling
835 between hedenbergite crystals; (D-F) Colloform pyrite (Py1) as veins cutting massive
836 pyrrhotite; (G-H) Colloform pyrite (Py1) vein cutting magnetite, and replaced by fine-grained
837 pyrite (Py3) and chalcopyrite (I); (J) Colloform pyrite (Py1) ore replaced by massive
838 sphalerite-galena; (K-L) Coarse-grained pyrite (Py2), sphalerite and calcite replace colloform
839 pyrite (Py1).
840
841 **Figure 8.** Summary of hydrothermal mineral paragenesis at Xinqiao deposit.
842
843 **Figure 9.** LA-ICP MS trace element maps of pyrite from stratabound (A, B) and porphyry ore
844 (C) from Xinqiao deposit.
845
846 **Figure 10.** Trace-element compositions of the studied pyrite samples from stratabound, skarn
847 and porphyry ore from the Xinqiao deposit (outline of pyrite data from porphyry Cu deposit,
848 SEDEX deposit and sedimentary from Mukherjee et al. (2017) and Gregory et al. 2019).
849 Colloform pyrite (Py1) is characterized by high abundances of Cu, Pb, Zn, Ag, Bi, W, Tl, and
850 Sb, and low Co, Ni, Se; Py4/4a have similar contents of Cu, Pb, Zn, Ag, Bi, W, Tl, and Sb as
851 Py1. In contrast, pyrite from the porphyry ore (Py6/7) is enriched in Co, Ni, Se.
852
853 **Figure 11.** Sulfur isotope compositions from the Xinqiao deposit. The $\delta^{34}S$ values of
854 Mesozoic magmatic rocks and sedimentary sulfides and sulfates from the Tongling district are
855 from Pan and Dong (1999); the $\delta^{34}S$ data of pyrite from typical Devonian-Carboniferous

856 SEDEX deposits are from the Carboniferous Red Dog deposit (Kelley et al. 2004) and the late
857 Devonian Dajiangping deposit (Qiu et al. 2018).
858
859 **Figure 12.** Representative LA-ICP-MS time-resolved signals of the Xinqiao pyrite.
860
861 **Figure 13.** Genetic model for the stratabound ore at Xinqiao. (A) Schematic model for
862 stratabound ore showing massive colloform ore (dark) and massive coarse-grained pyrite ore
863 (yellow); (B) later magmatic-hydrothermal fluid (enriched in Co, Ni, and As) forms the
864 massive coarse-grained pyrite (Py2) and fine-grained pyrite (Py3) with chalcopyrite, and
865 overprints colloform pyrite (Py1); (C) early magmatic-hydrothermal fluid (enriched in base
866 metals) migrate along Carboniferous-Devonian detachment surface and formed colloform
867 pyrite (Py1).
868
869 **Figure 14.** Element concentration scatterplots for pyrite from stratabound, skarn and
870 porphyry ore in MLYB (data source from Wang (2015), Zhang et al. (2017), Du et al. (2020),
871 Han (2020); Xie et al. (2020a, b)). (A) Co versus Ni; (B) Co+Ni versus As+Sb+Pb+Ag+Bi;
872 (C) Co versus As/Se; (D) Co/Cu versus Ag/Co. Field for Northern Chile from (Herazo et al.
873 2021)
874 **Table Captions**
875 Appendix Table 1A. In situ trace elements of pyrite from Xinqiao deposit.
876 Appendix Table 2A. In situ sulfur isotope data of pyrite (from regional sedimentary rock) and
877 sulfides from Xinqiao deposit.

Figure 1

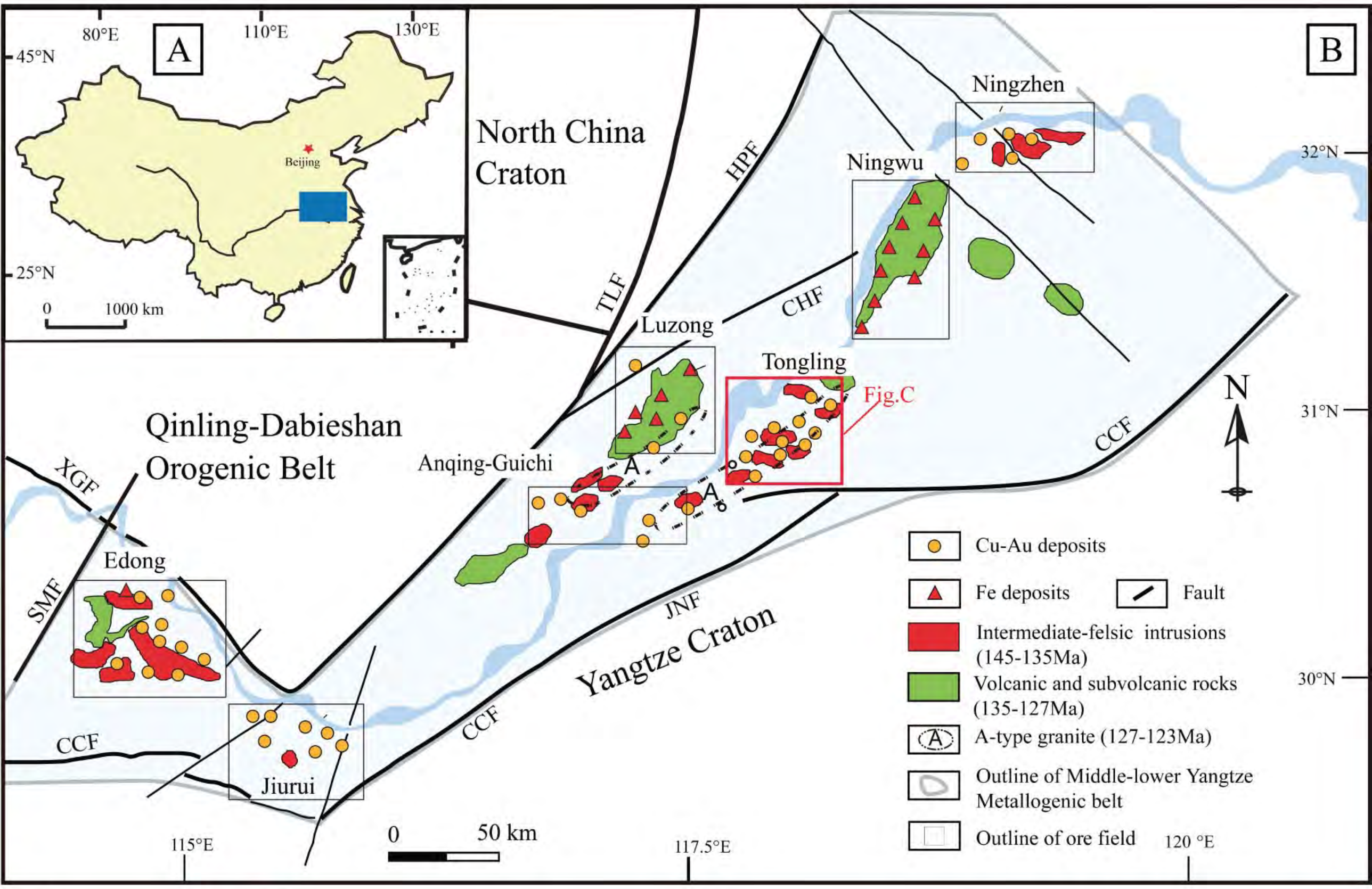
A
80°E
110°E
130°E
45°N
25°N
Beijing
0
1000 km
B
North China
Craton
HPF
TLF
CHF
Ningzhen
Ningwu
Luzong
Tongling
Fig.C
N
31°N
Qinling-Dabieshan
Orogenic Belt
XGF
SMF
Edong
Anqing-Guichi
A
CCF
JNF
Yangtze Craton
Jiurui
30°N
Cu-Au deposits
Fe deposits
Fault
Intermediate-felsic intrusions
(145-135Ma)
Volcanic and subvolcanic rocks
(135-127Ma)
A-type granite (127-123Ma)
Outline of Middle-lower Yangtze
Metallogenic belt
Outline of ore field
115°E
117.5°E
120 °E
0
50 km

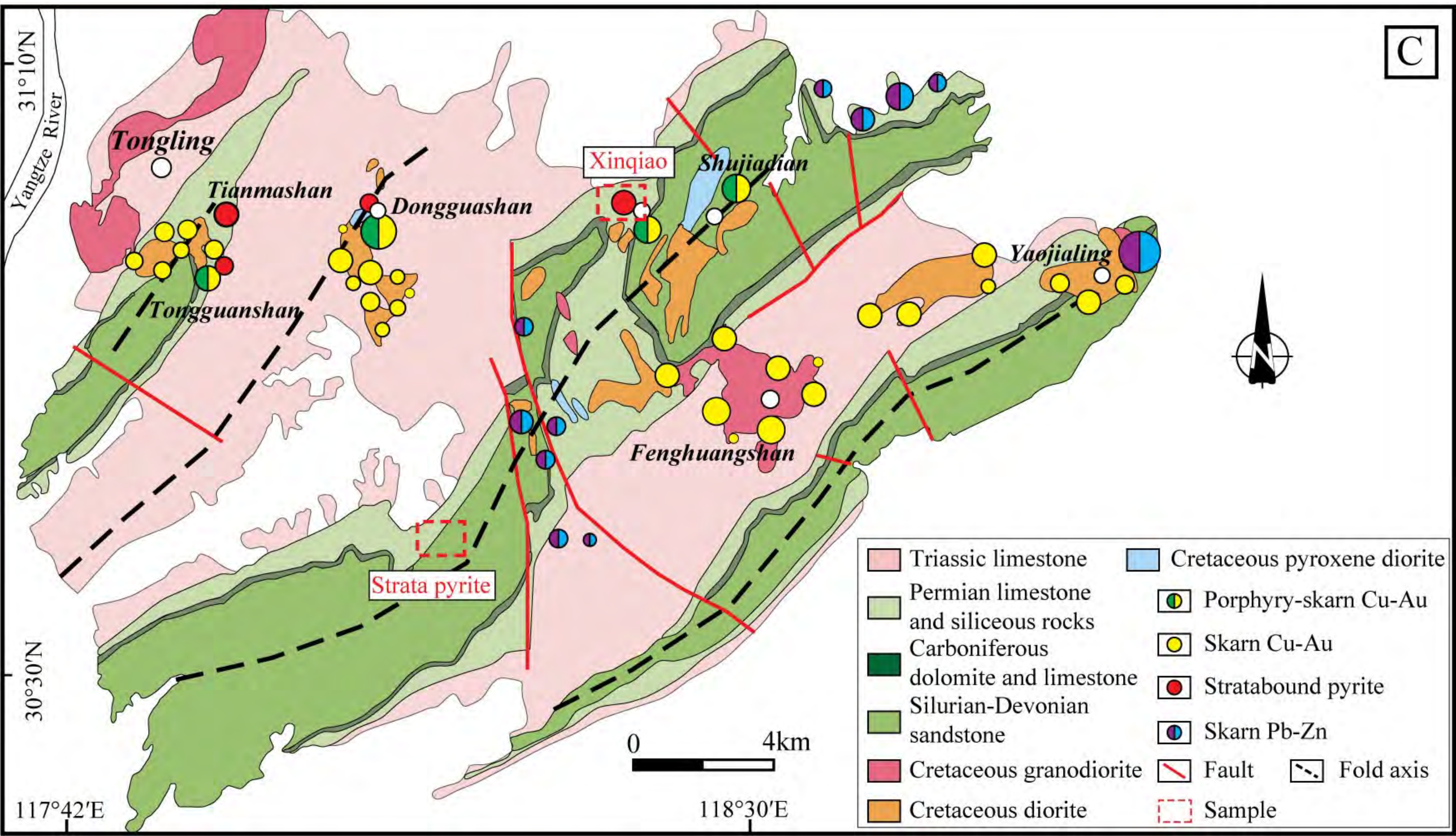
C
31°10′N
Yangtze River
Tongling
Tianmashan
Dongguashan
Tongguanshan
Xinqiao
Shujiadian
Yaojialing
Fenghuangshan
Strata pyrite
30°30′N
0
4km
117°42′E
118°30′E
Triassic limestone
Permian limestone
and siliceous rocks
Carboniferous
dolomite and limestone
Silurian-Devonian
sandstone
Cretaceous granodiorite
Cretaceous diorite
Cretaceous pyroxene diorite
Porphyry-skarn Cu-Au
Skarn Cu-Au
Stratabound pyrite
Skarn Pb-Zn
Fault
Fold axis
Sample

Figure 2

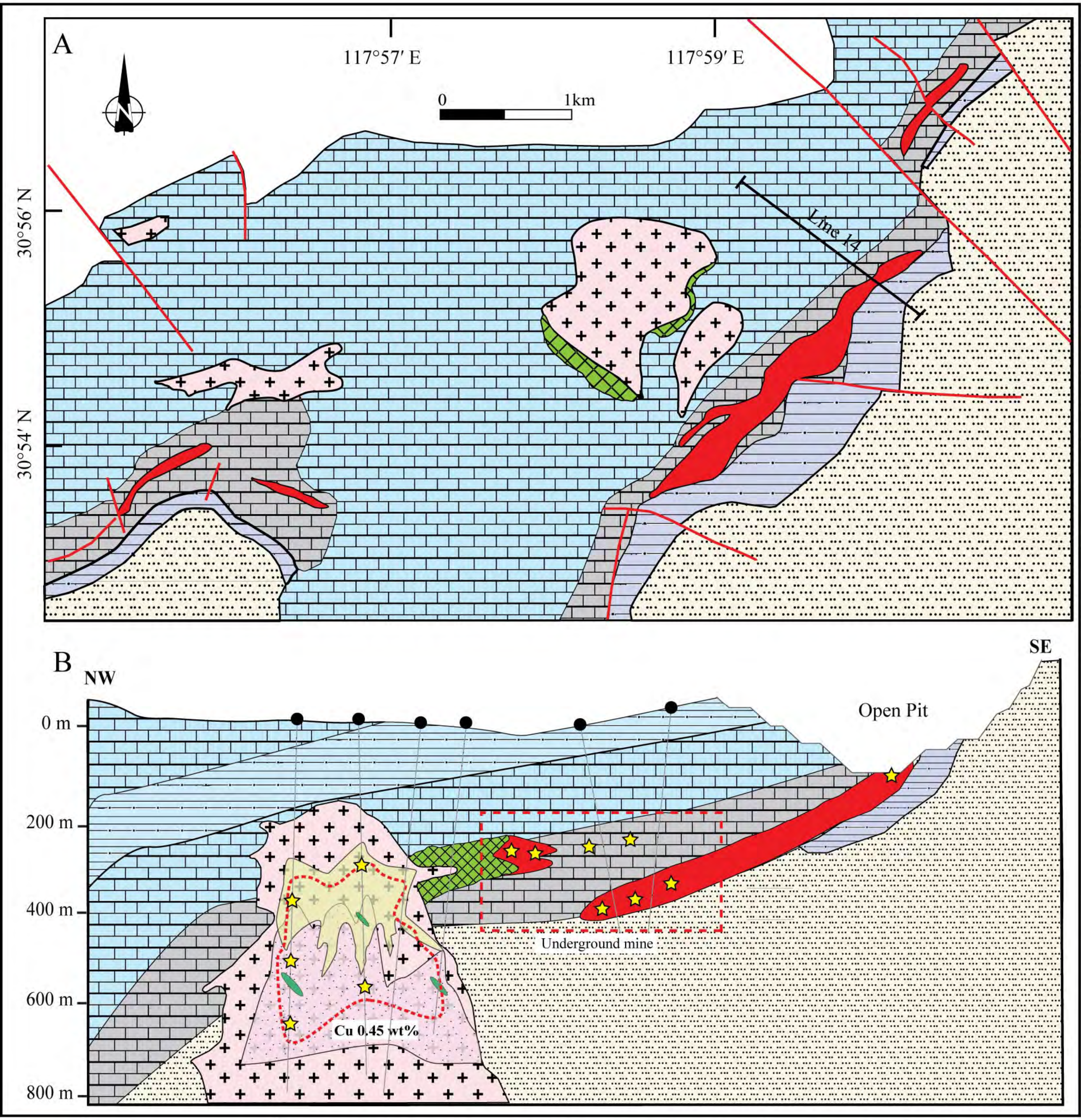
A
117°57′ E
117°59′ E
0
1km
30°56′ N
30°54′ N
Line 14
B
NW
SE
0 m
200 m
400 m
600 m
800 m
Open Pit
Underground mine
Cu 0.45 wt%
Permian limestone
Permian mudstones & siltstones
Carboniferous limestone & dolomite limestone
Carboniferous silty shale & siltstones
Devonian Sandstone
Jitou stock (Quartz monzodiorite)
Potassic zone
Phyllic zone
Epidote-chlorite zone
Skarn
Porphyry ore
Orebody
Samples
Fault

Figure 3

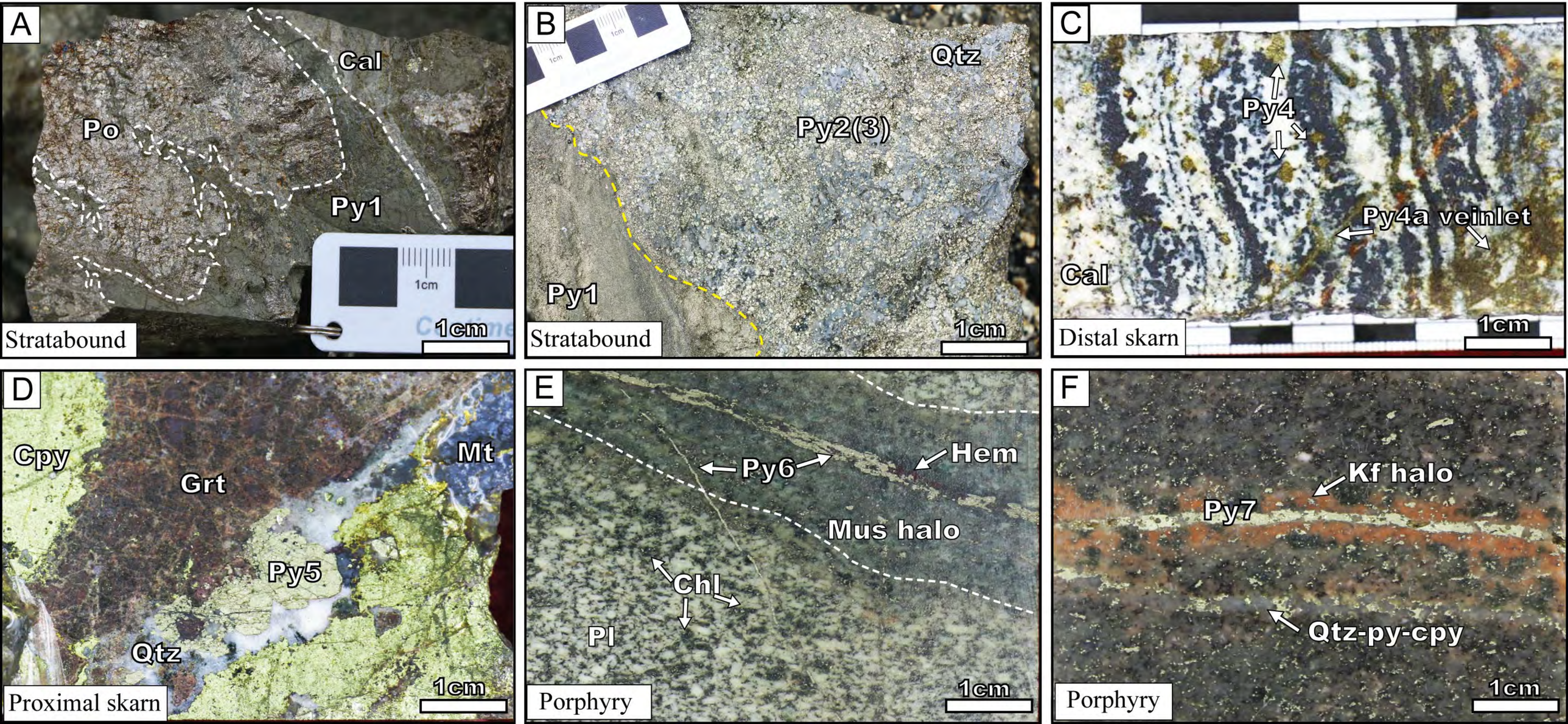
A
Cal
Po
Py1
1cm
Stratabound
B
Qtz
Py2(3)
Py1
Stratabound
1cm
C
Py4
Py4a veinlet
Cal
Distal skarn
1cm
D
Cpy
Grt
Mt
Py5
Qtz
Proximal skarn
1cm
E
Py6
Hem
Mus halo
Chl
Pl
Porphyry
1cm
F
Kf halo
Py7
Qtz-py-cpy
Porphyry
1cm

Figure 4

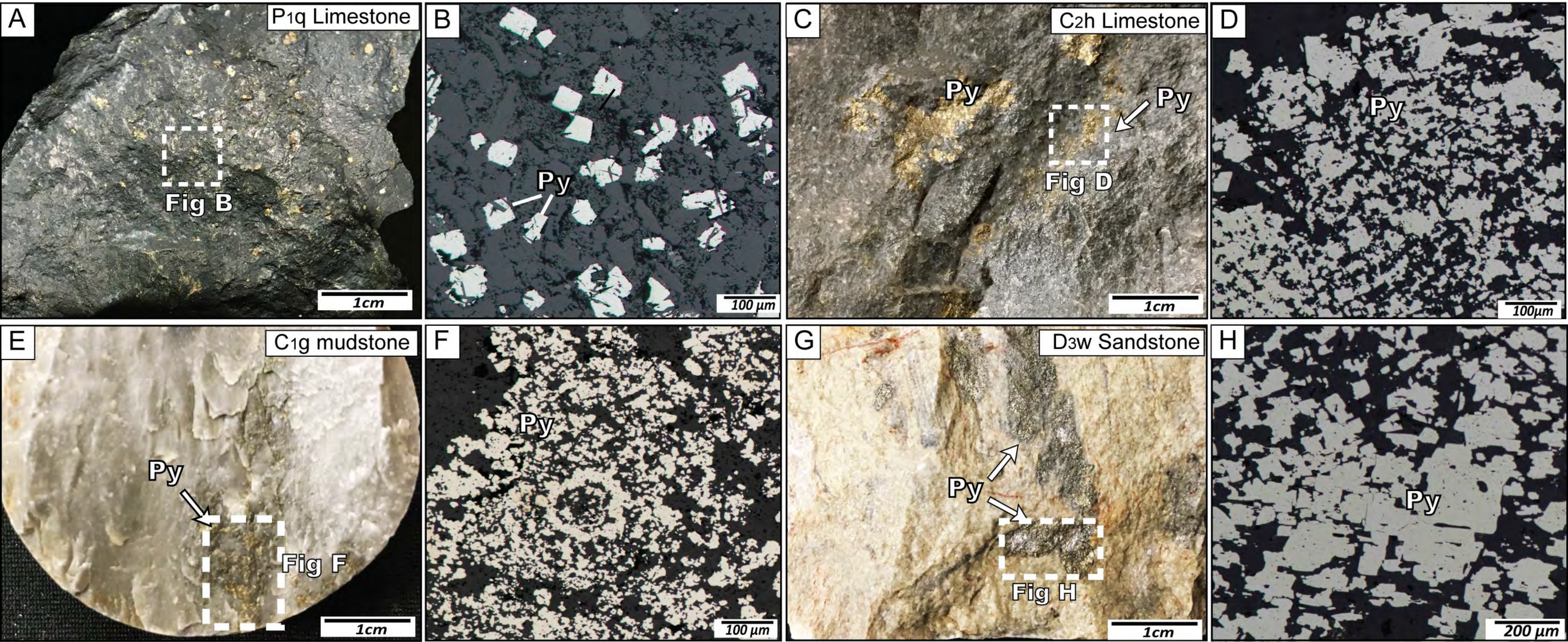
A
P1q Limestone
Fig B
1cm
B
Py
100 μm
C
C2h Limestone
Py
Py
Fig D
1cm
D
Py
100μm
E
C1g mudstone
Py
Fig F
1cm
F
Py
100 μm
G
D3w Sandstone
Py
Fig H
1cm
H
Py
200 μm

Figure 5

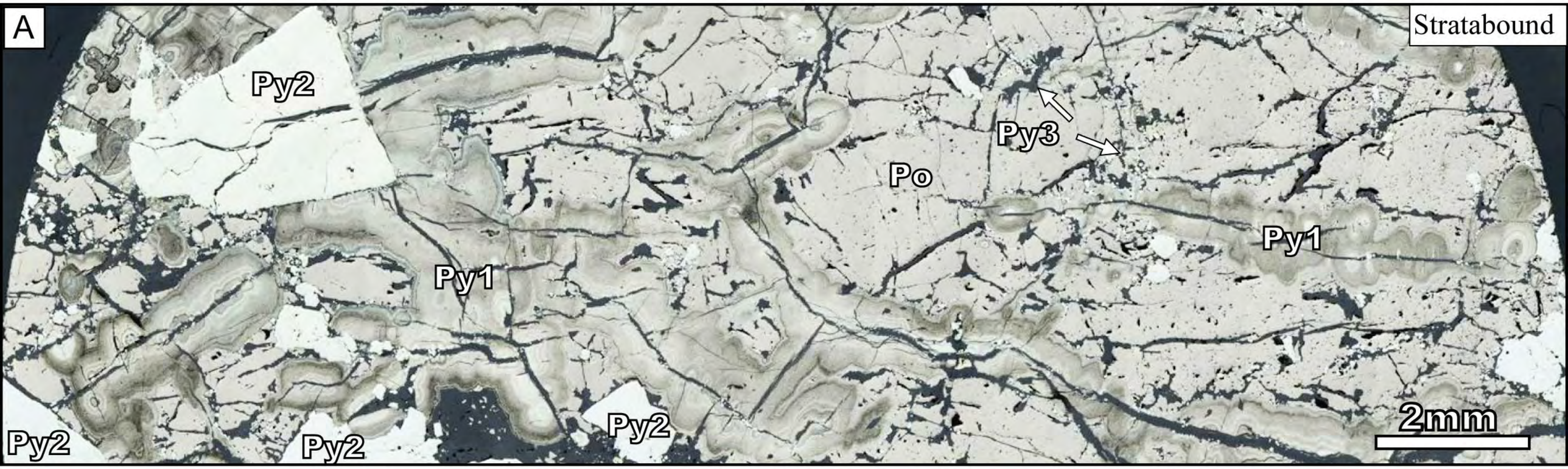
A
Stratabound
Py2
Py3
Po
Py1
Py1
Py2
Py2
Py2
2mm
B
Qtz
Py3
Py1
Py1
Cpy
Stratabound
C
Py1
Py2
Stratabound
D
Py2
Py1
Stratabound
E
Py1
Po
Py3
Stratabound
F
Py4
Py4a
Marble
G
Qtz
Py5
Cpy
Skarn ore
200μm
H
Qtz
Py6
Porphyry ore
I
Mo
Py7
Qtz
Porphyry ore

Figure 6

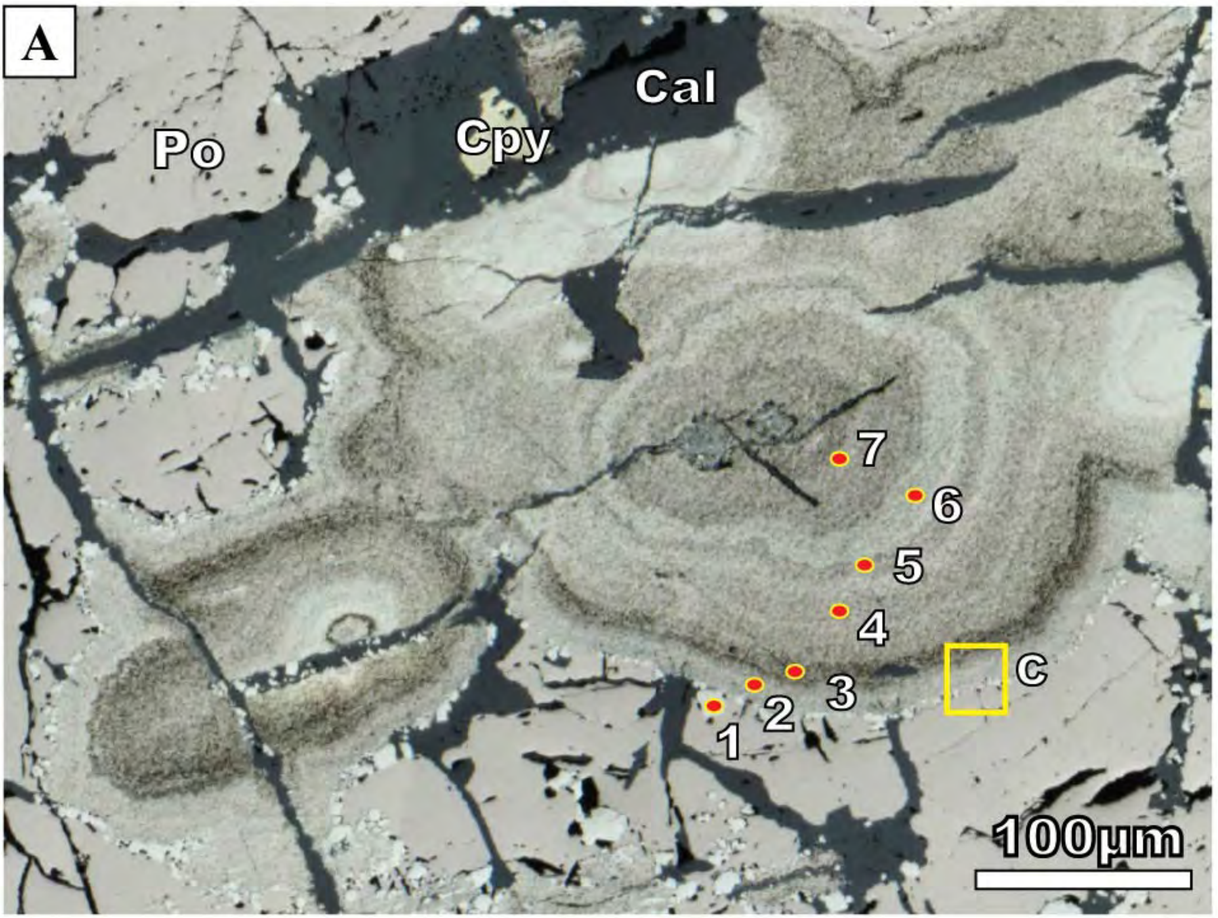
A
Po
Cpy
Cal
7
6
5
4
3
2
1
C
100μm

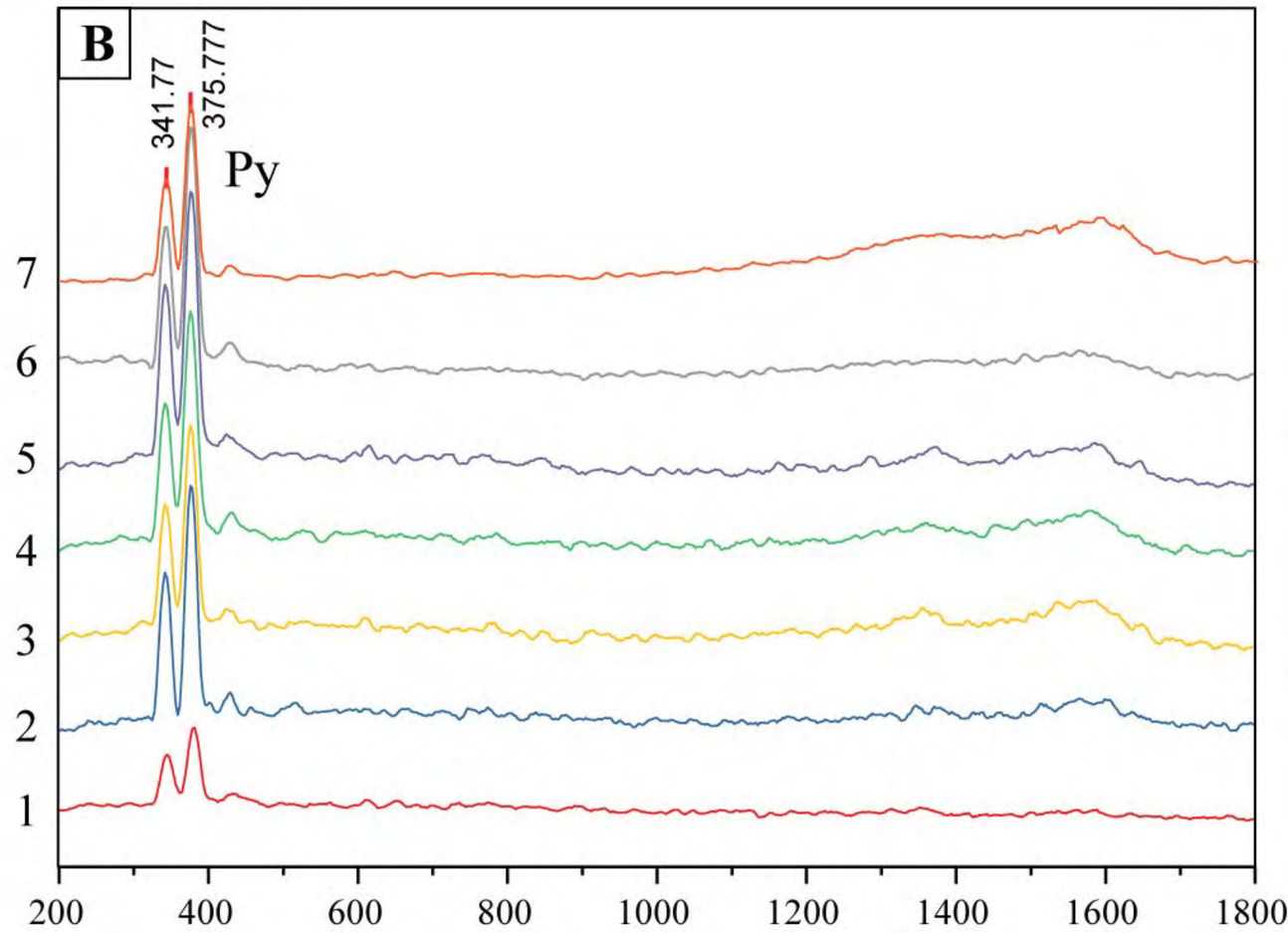
B
341.77
375.777
Py
7
6
5
4
3
2
1
200
400
600
800
1000
1200
1400
1600
1800

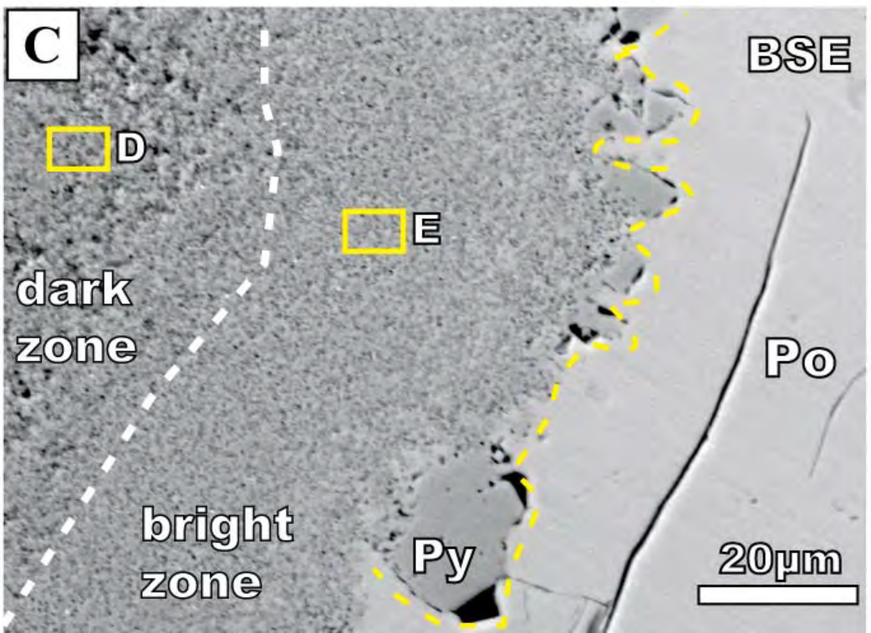
C
BSE
D
E
dark
zone
bright
zone
Py
Po
20μm

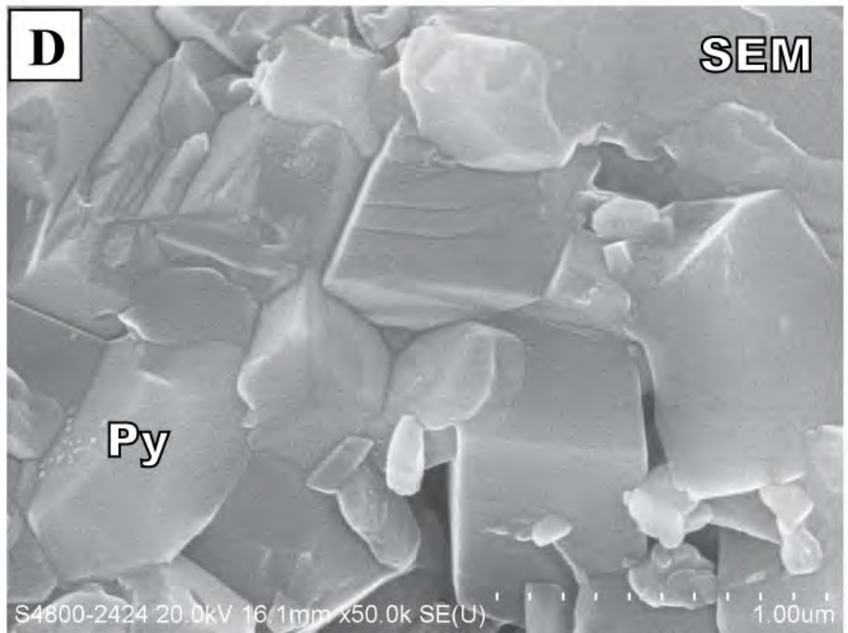
D
SEM
Py
S4800-2424 20.0kV 16.1mm x50.0k SE(U)
1.00um

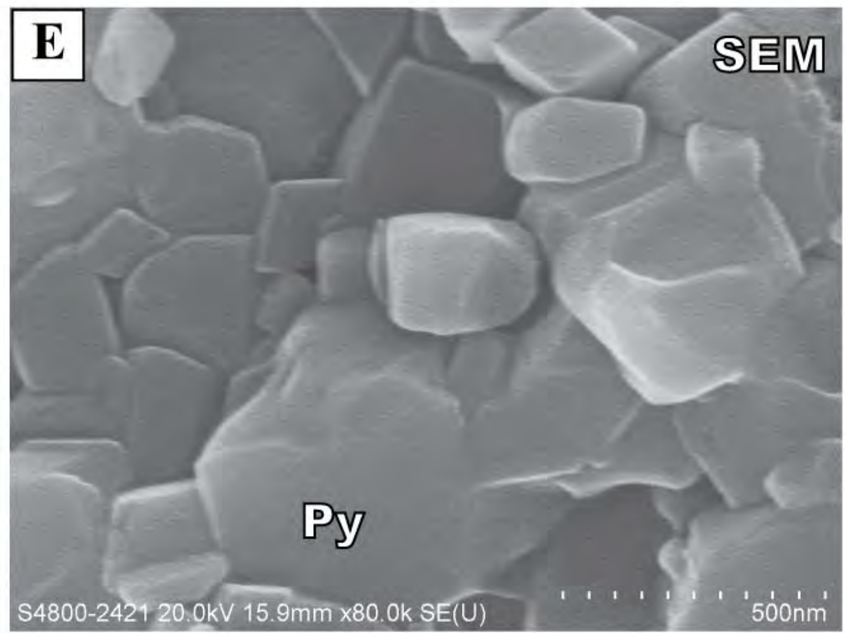
E
SEM
Py
S4800-2421 20.0kV 15.9mm x80.0k SE(U)
500nm

Figure 7

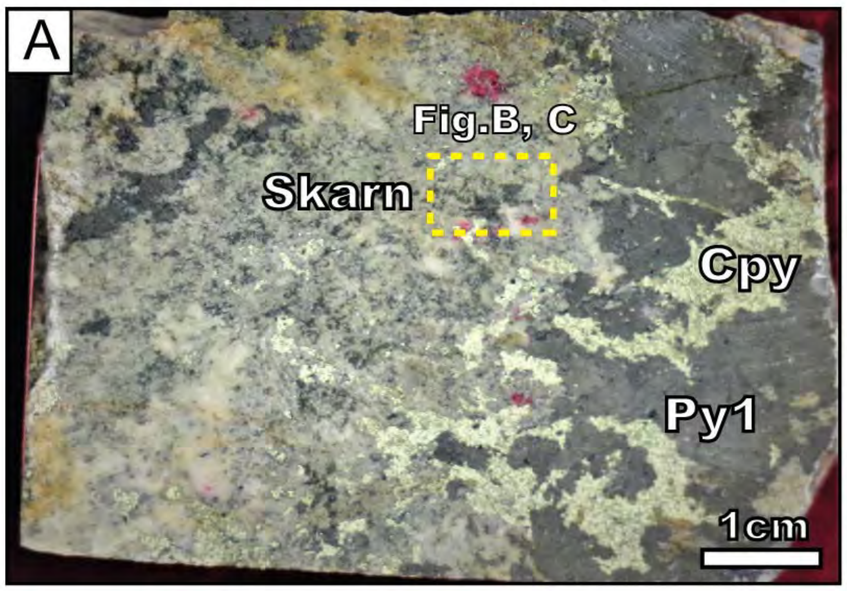
A
Fig.B, C
Skarn
Cpy
Py1
1cm

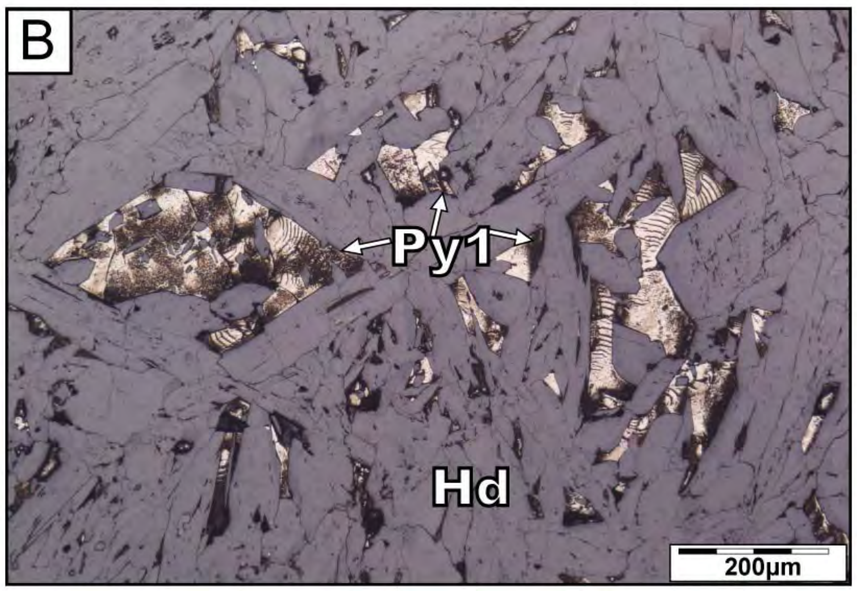
B
Py1
Hd
200μm

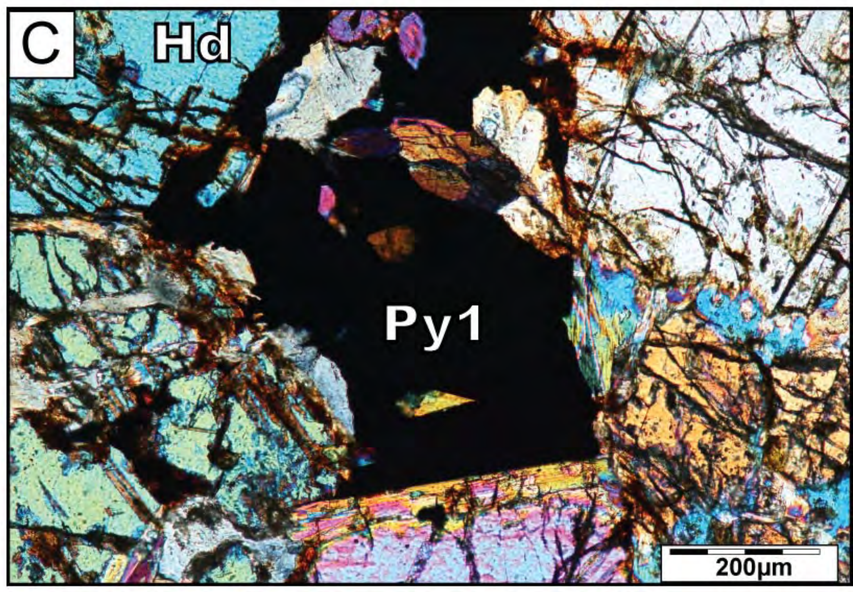
C
Hd
Py1
200μm

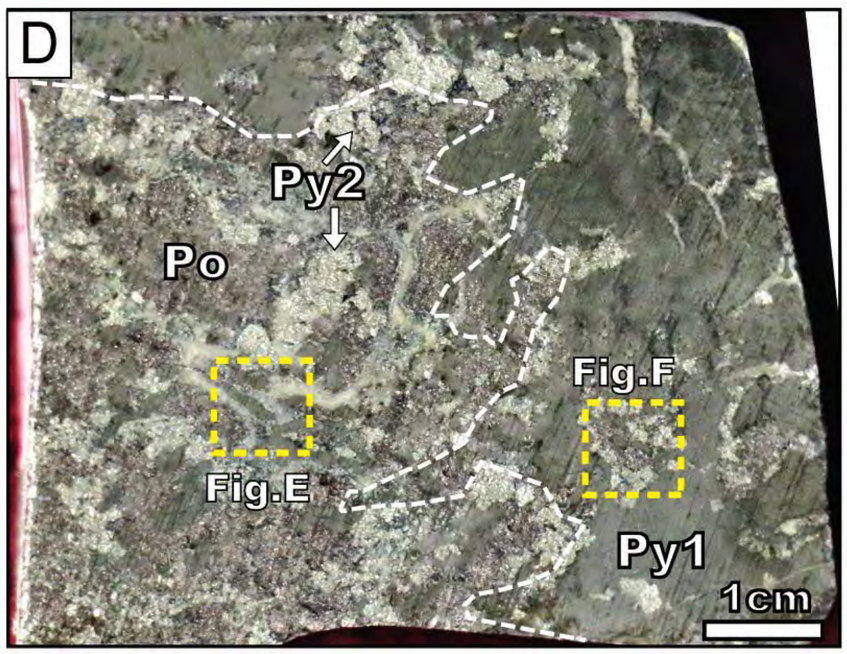
D
Py2
Po
Fig.F
Fig.E
Py1
1cm

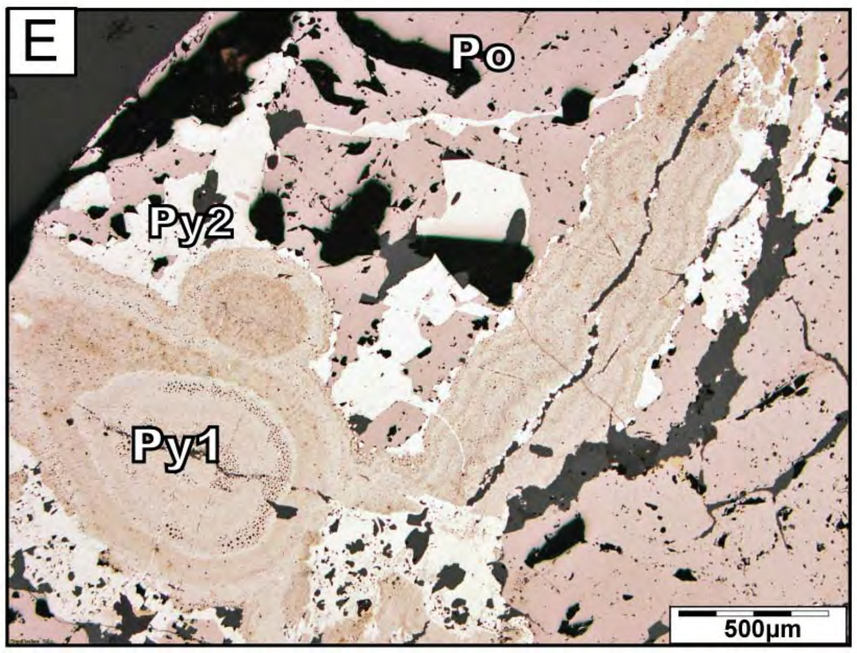
E
Po
Py2
Py1
500μm

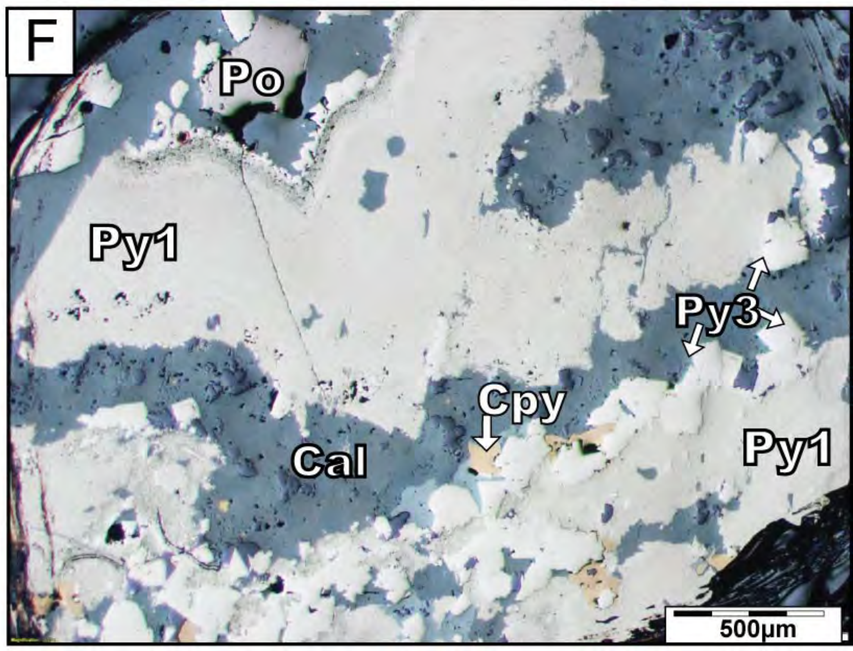
F
Po
Py1
Py3
Cpy
Cal
Py1
500μm

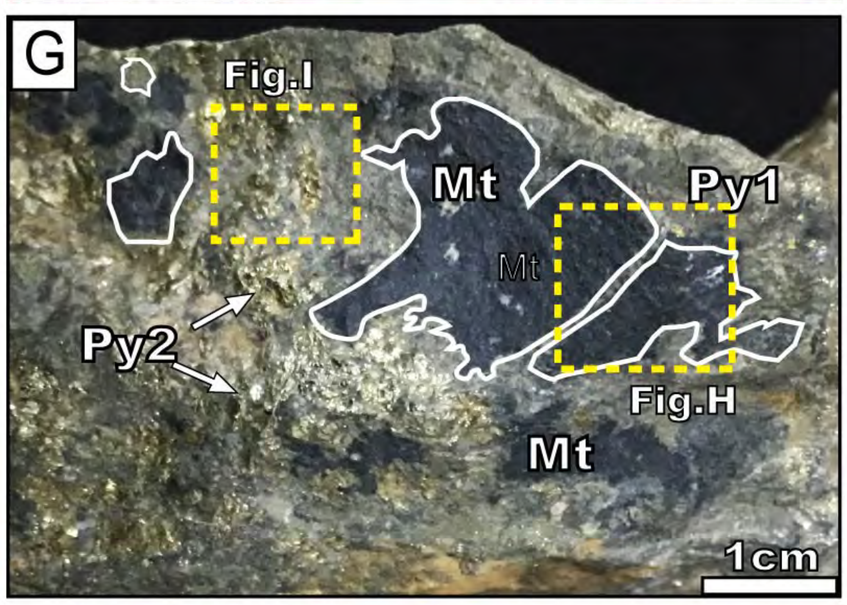
G
Fig.I
Mt
Py1
Mt
Py2
Fig.H
Mt
1cm

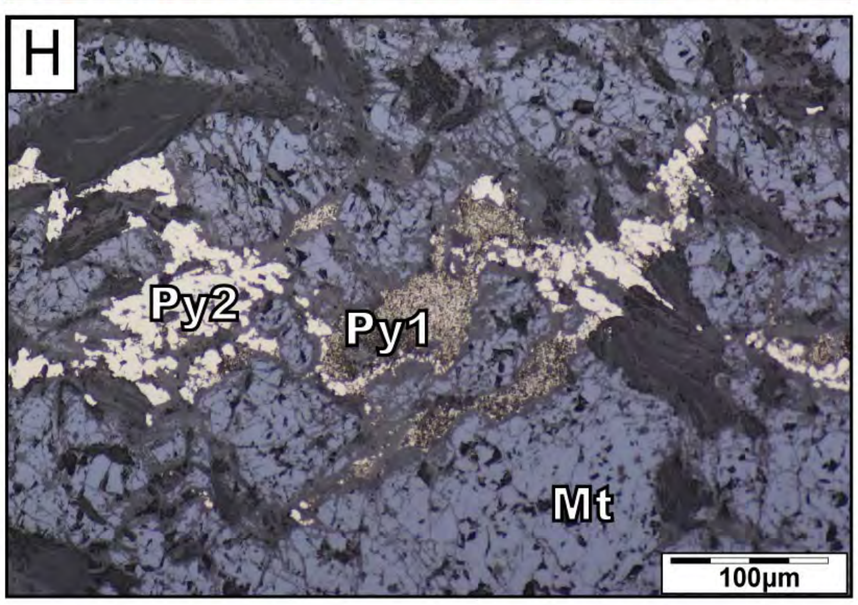
H
Py2
Py1
Mt
100μm

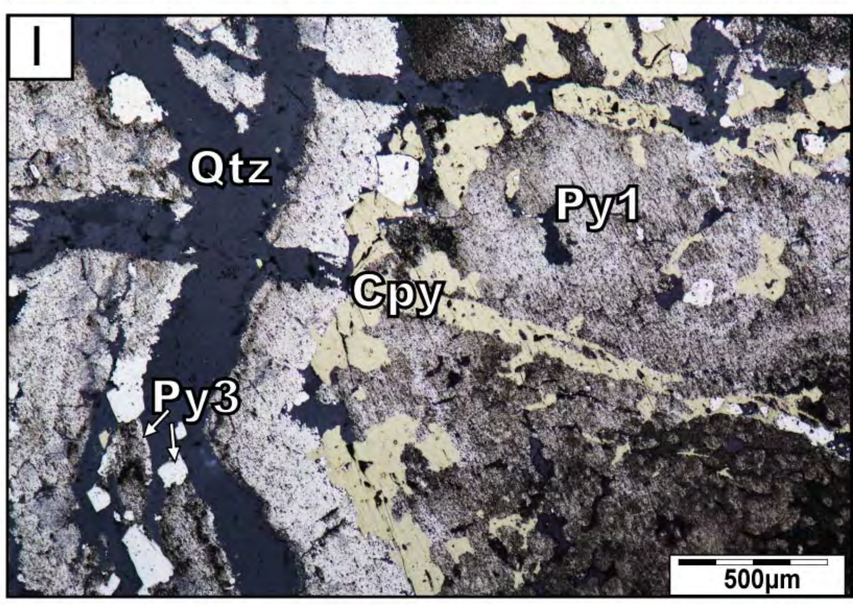
I
Qtz
Py1
Cpy
Py3
500μm

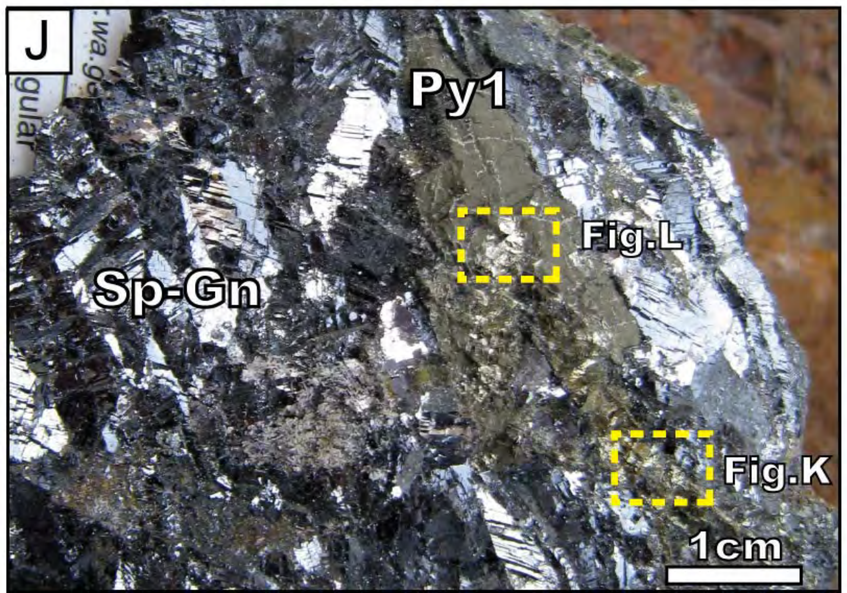
J
Py1
Fig.L
Sp-Gn
Fig.K
1cm

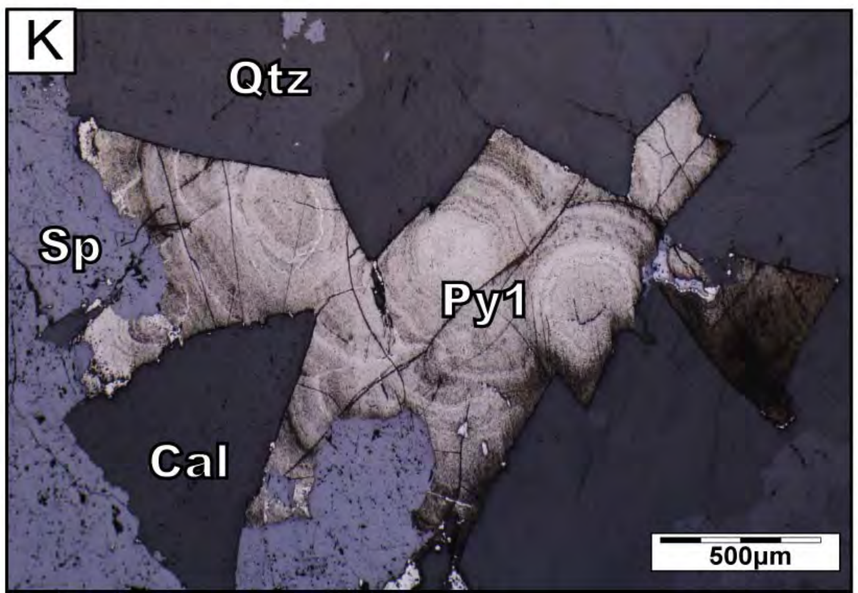
K
Qtz
Sp
Py1
Cal
500μm

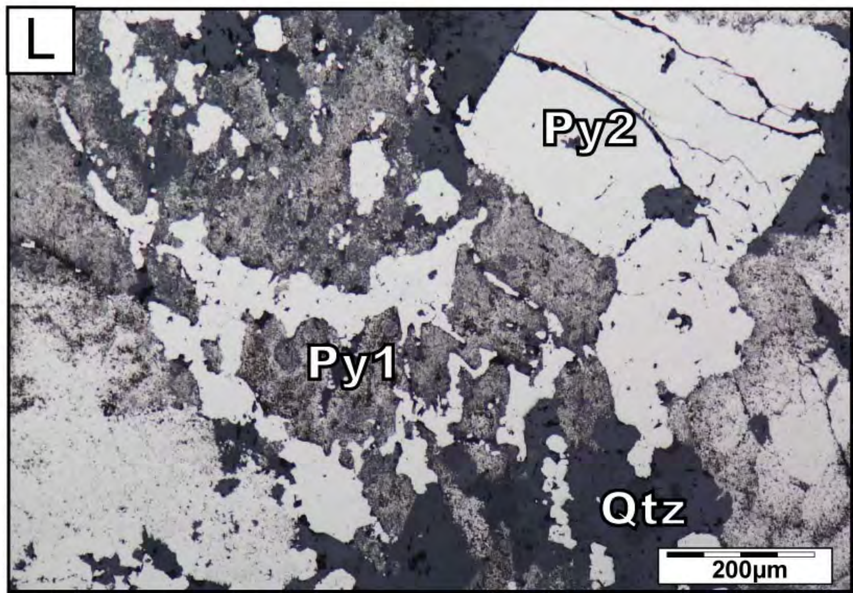
L
Py2
Py1
Qtz
200μm

Figure 8

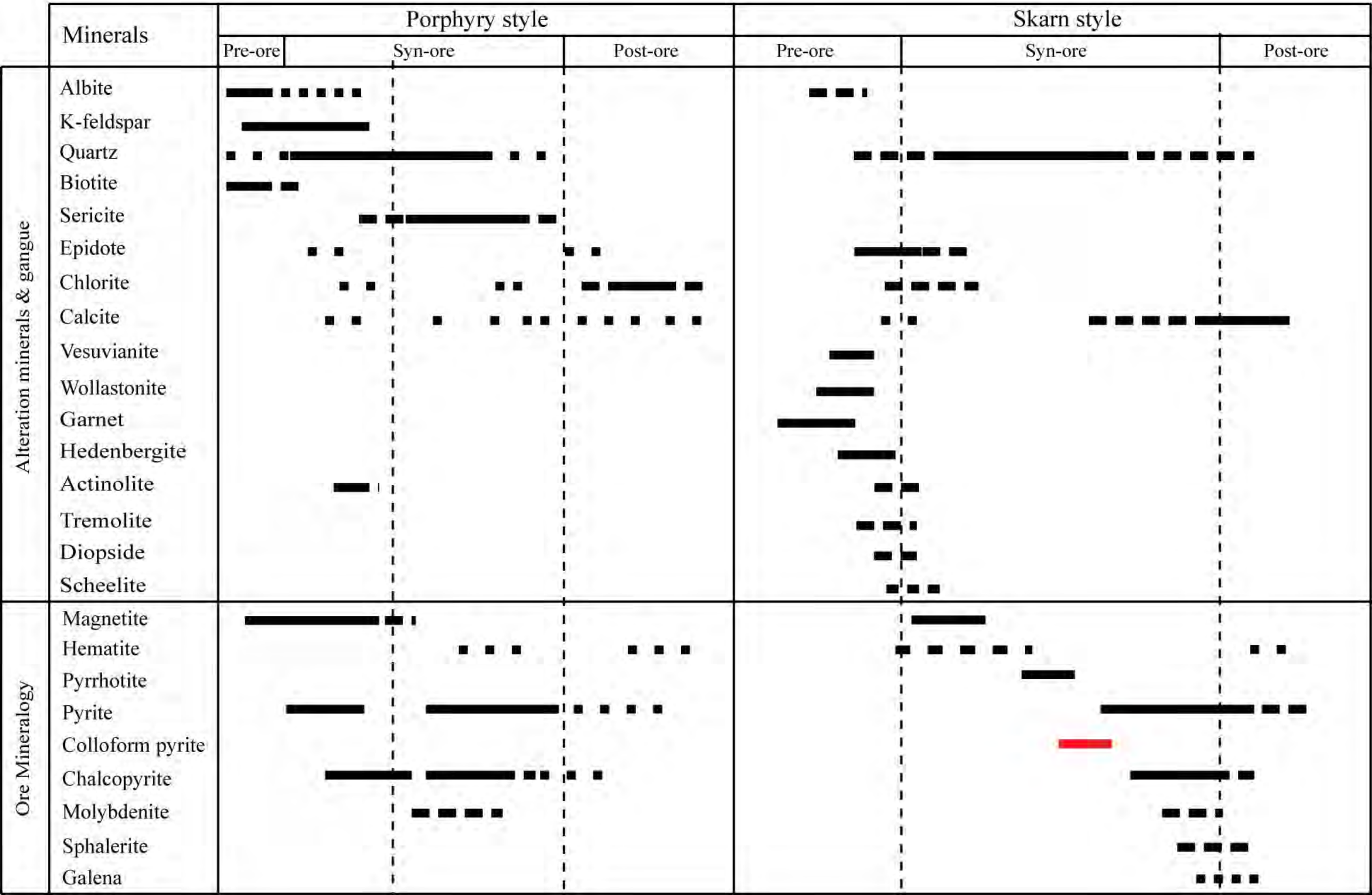
Minerals
Porphyry style
Skarn style
Pre-ore
Syn-ore
Post-ore
Pre-ore
Syn-ore
Post-ore
Alteration minerals & gangue
Albite
K-feldspar
Quartz
Biotite
Sericite
Epidote
Chlorite
Calcite
Vesuvianite
Wollastonite
Garnet
Hedenbergite
Actinolite
Tremolite
Diopside
Scheelite
Ore Mineralogy
Magnetite
Hematite
Pyrrhotite
Pyrite
Colloform pyrite
Chalcopyrite
Molybdenite
Sphalerite
Galena

Figure 9

A

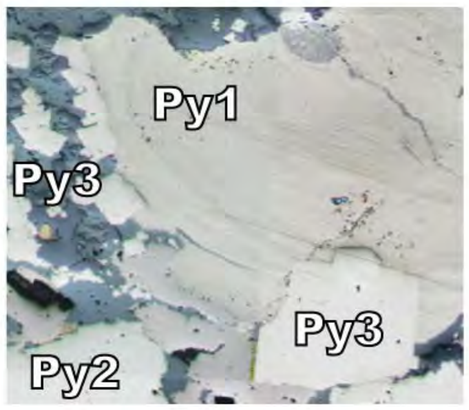

Stratabound ore

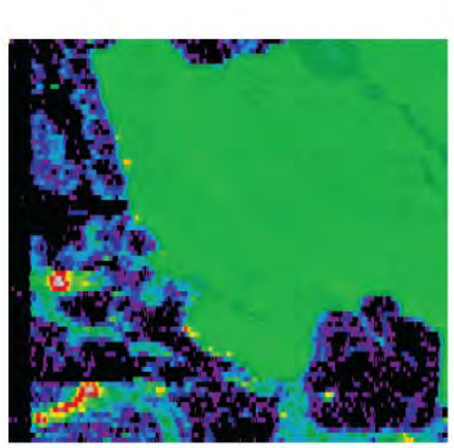

10^7 10^6 10^5 10^4 10^3 10^2

Cu65 cps

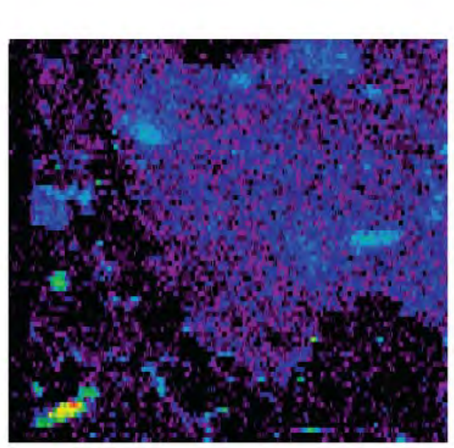

10^5 10^4 10^3 10^2

Zn66 cps

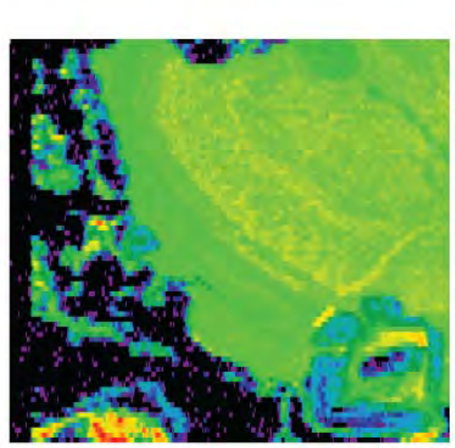

10^5 10^4 10^3 10^2

As75 cps

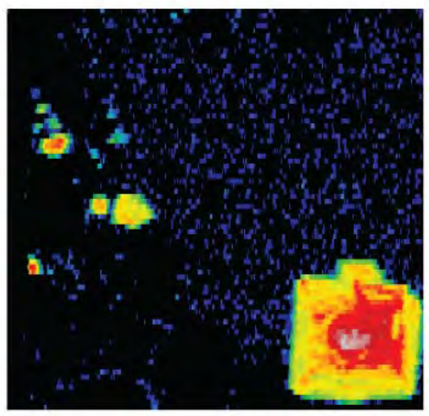

10^5 10^4 10^3 10^2

Co59 cps

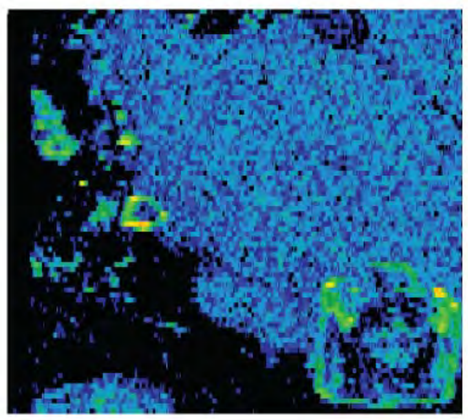

10^5 10^4 10^3 10^2

Ni60 cps

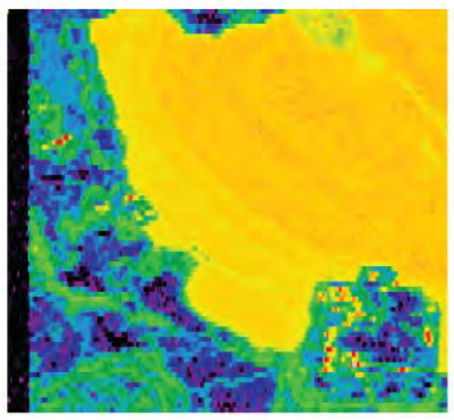

10^7 10^6 10^5 10^4 10^3 10^2

Pb208 cps

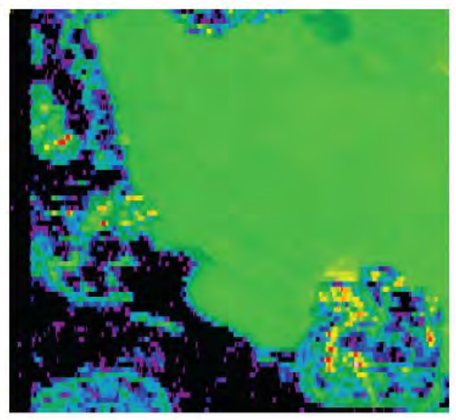

10^6 10^5 10^4 10^3 10^2

Bi209 cps

B

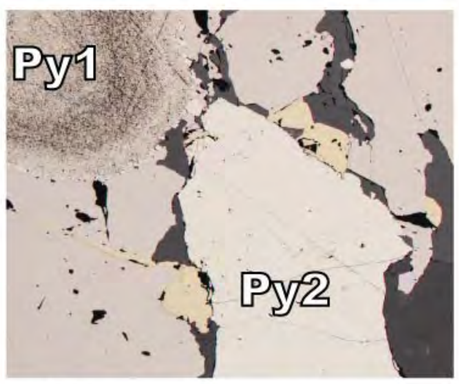

Stratabound ore

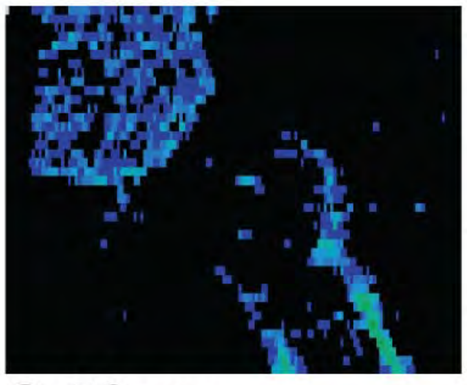

10^5 10^4 10^3 10^2

Co59 cps

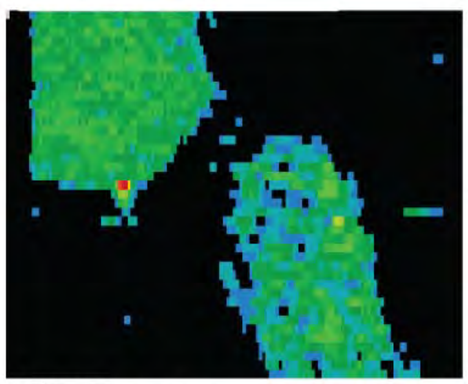

10^5 10^4 10^3 10^2

Ni60 cps

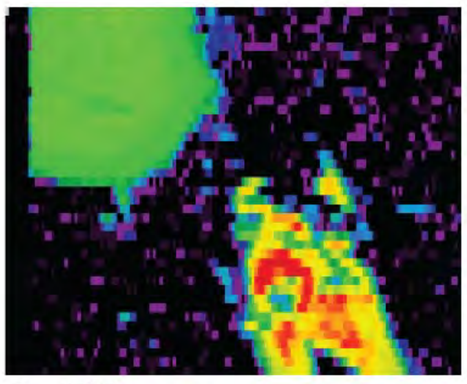

10^6 10^5 10^4 10^3

As75 cps

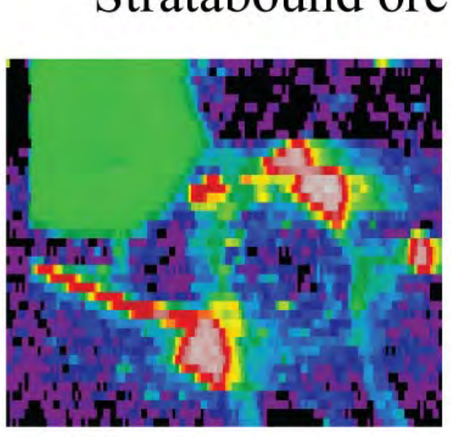

10^7 10^6 10^5 10^4 10^3 10^2

Cu65 cps

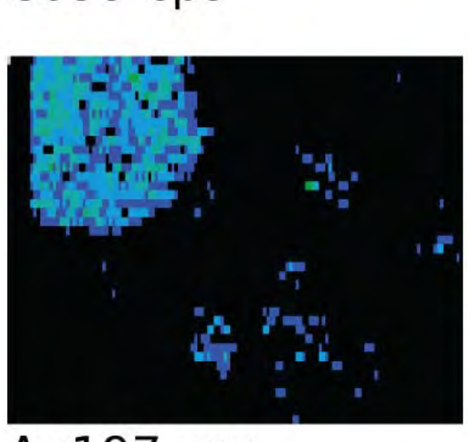

10^4 10^3 10^2 10^1

Au197 cps

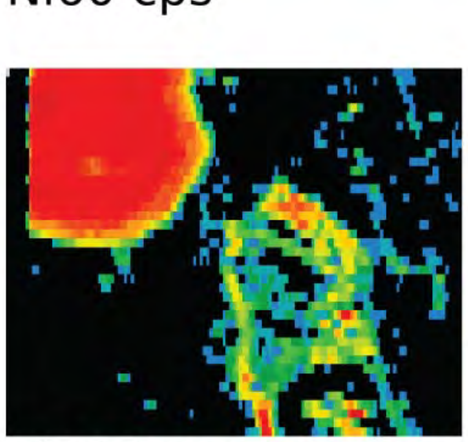

10^5 10^4 10^3 10^2

Bi209 cps

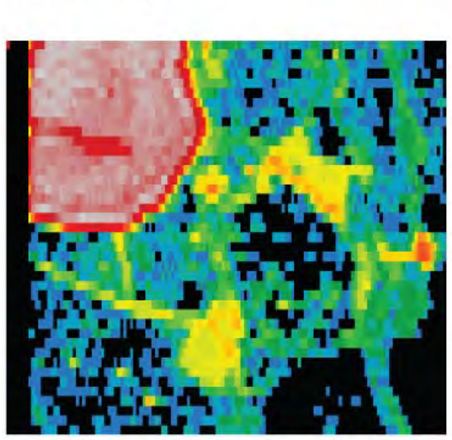

10^5 10^4 10^3 10^2

Ag107 cps

C

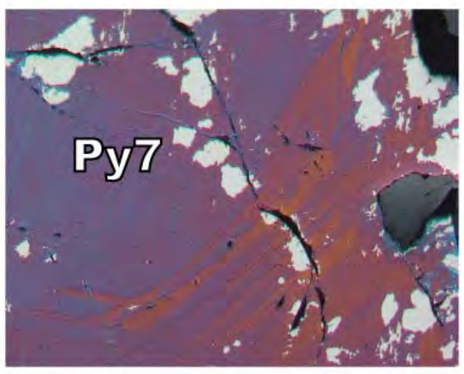

Porphyry ore

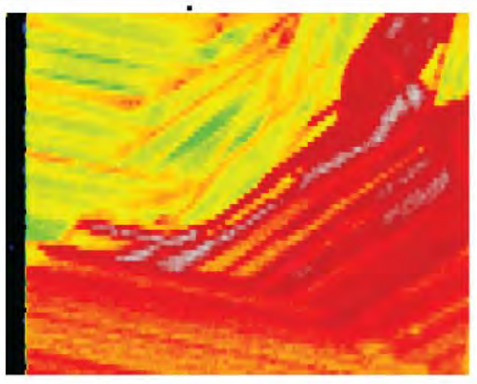

10^6 10^5 10^4 10^3 10^2

Co59 cps

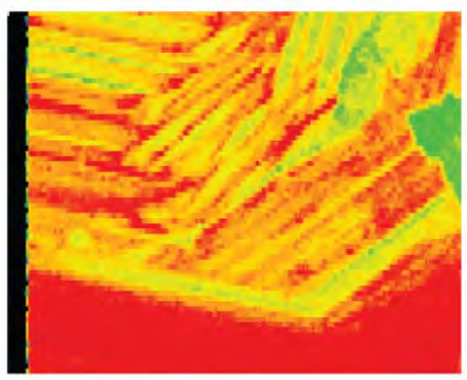

10^5 10^4 10^3 10^2

Ni60 cps

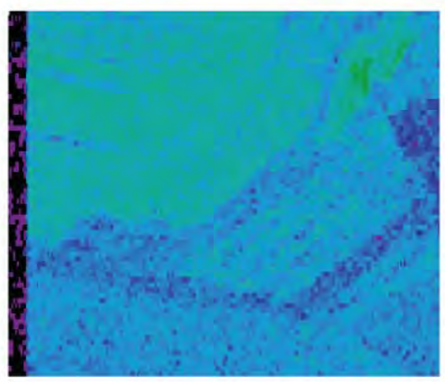

10^5 10^4 10^3 10^2

Se77 cps

Figure 10

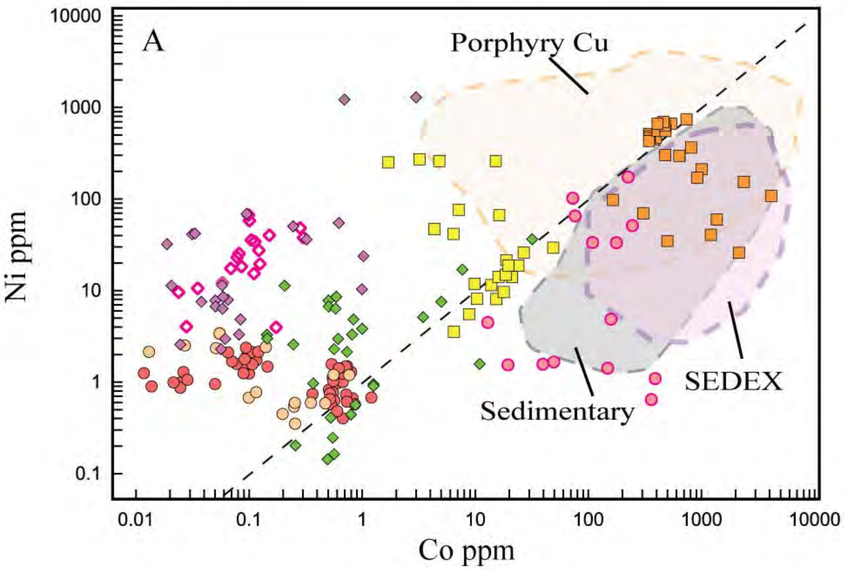

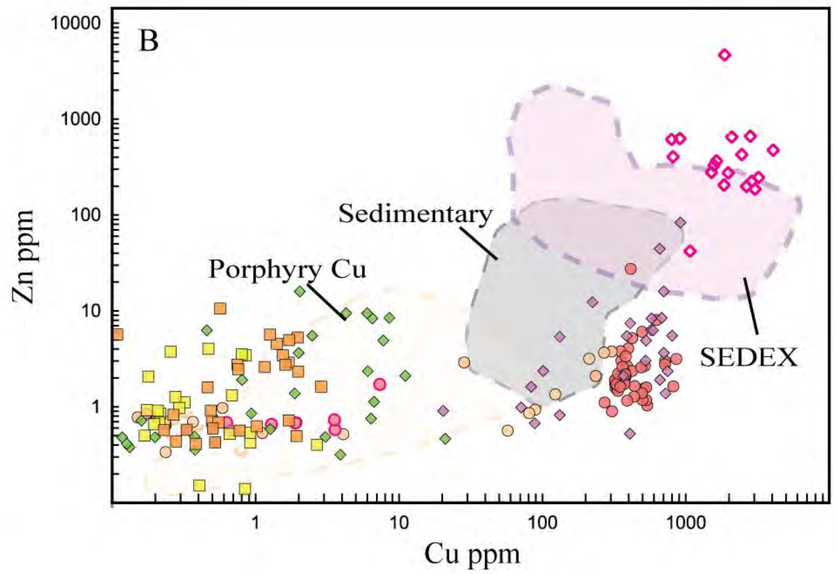

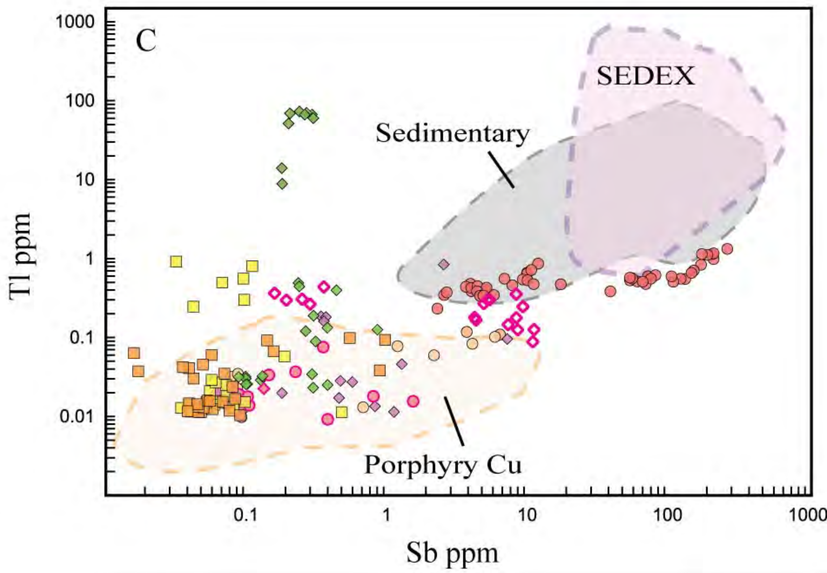

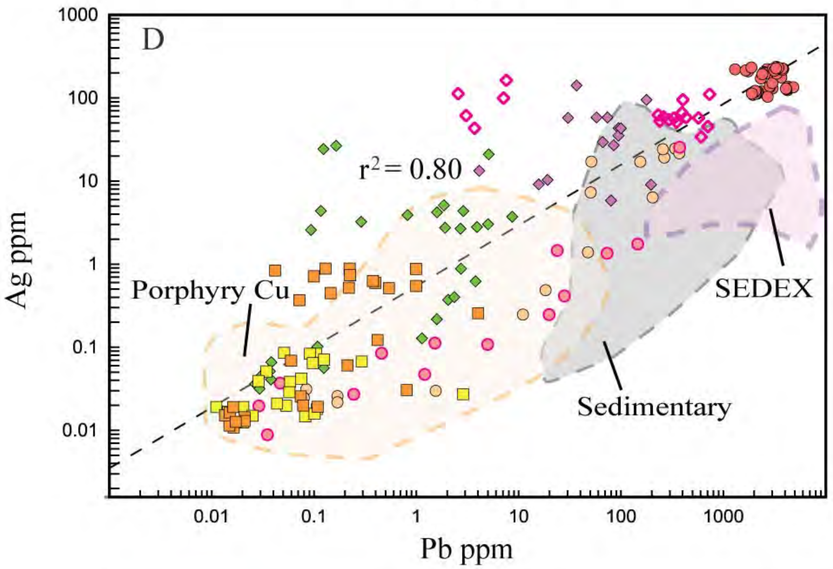

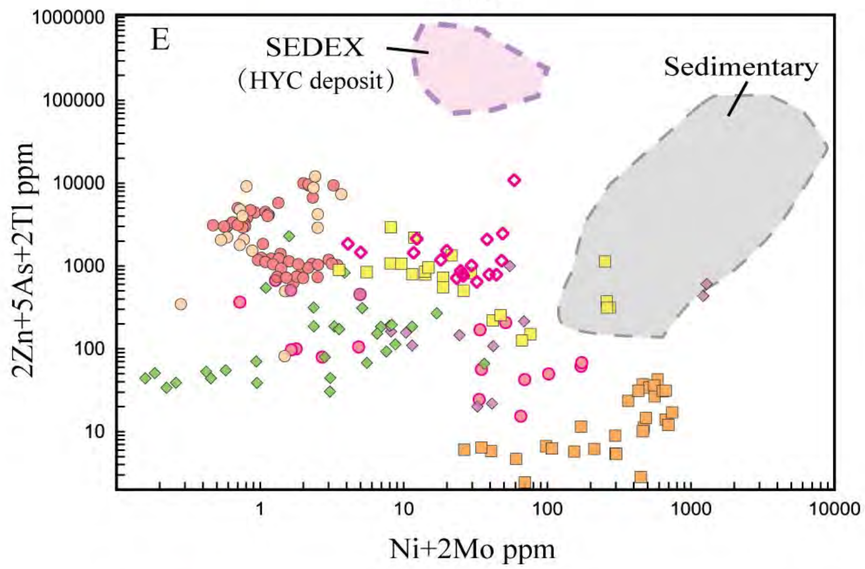

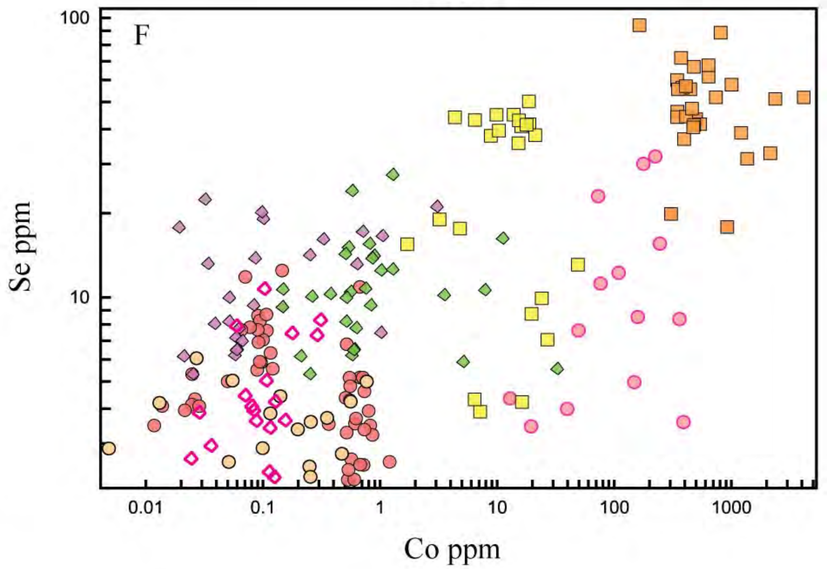

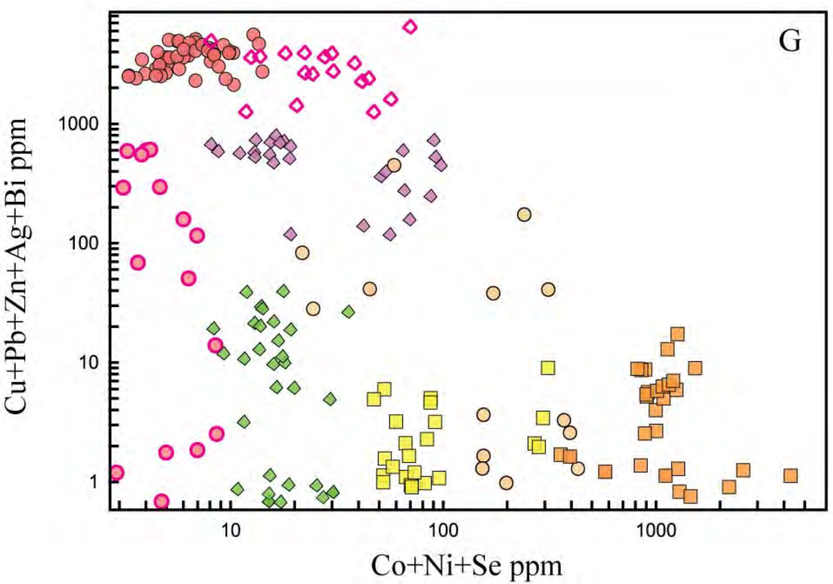

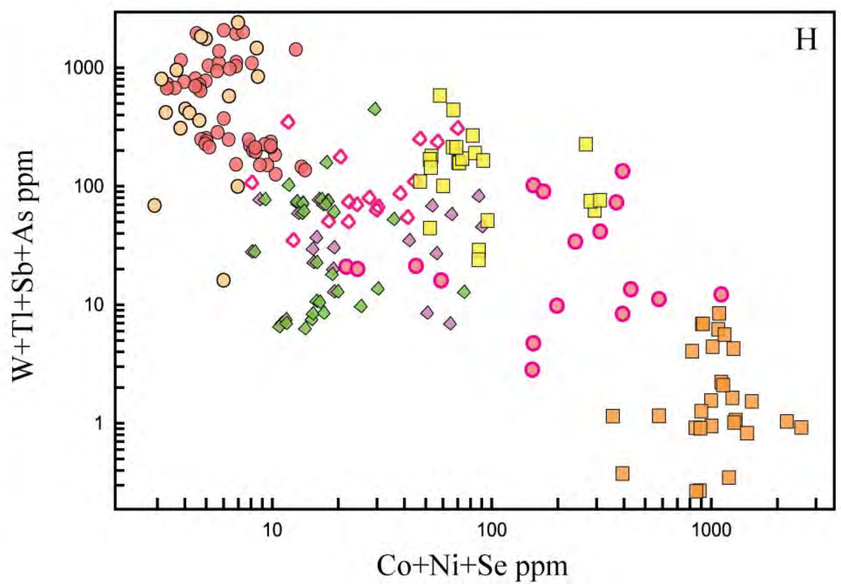

Stratabound ore
- Py1 colloform pyrite
- Py2 coarse-grained pyrite
- Py3 fine-grained pyrite

Skarn ore
- Py4a fine-grained pyrite in marble
- Py4 coarse-grained pyrite in marble
- Py5 coarse-grained pyrite in massive ore

Porphyry ore
- Py6 pyrite in phyllic alteration zone
- Py7 pyrite in potassic alteration zone

Figure 11

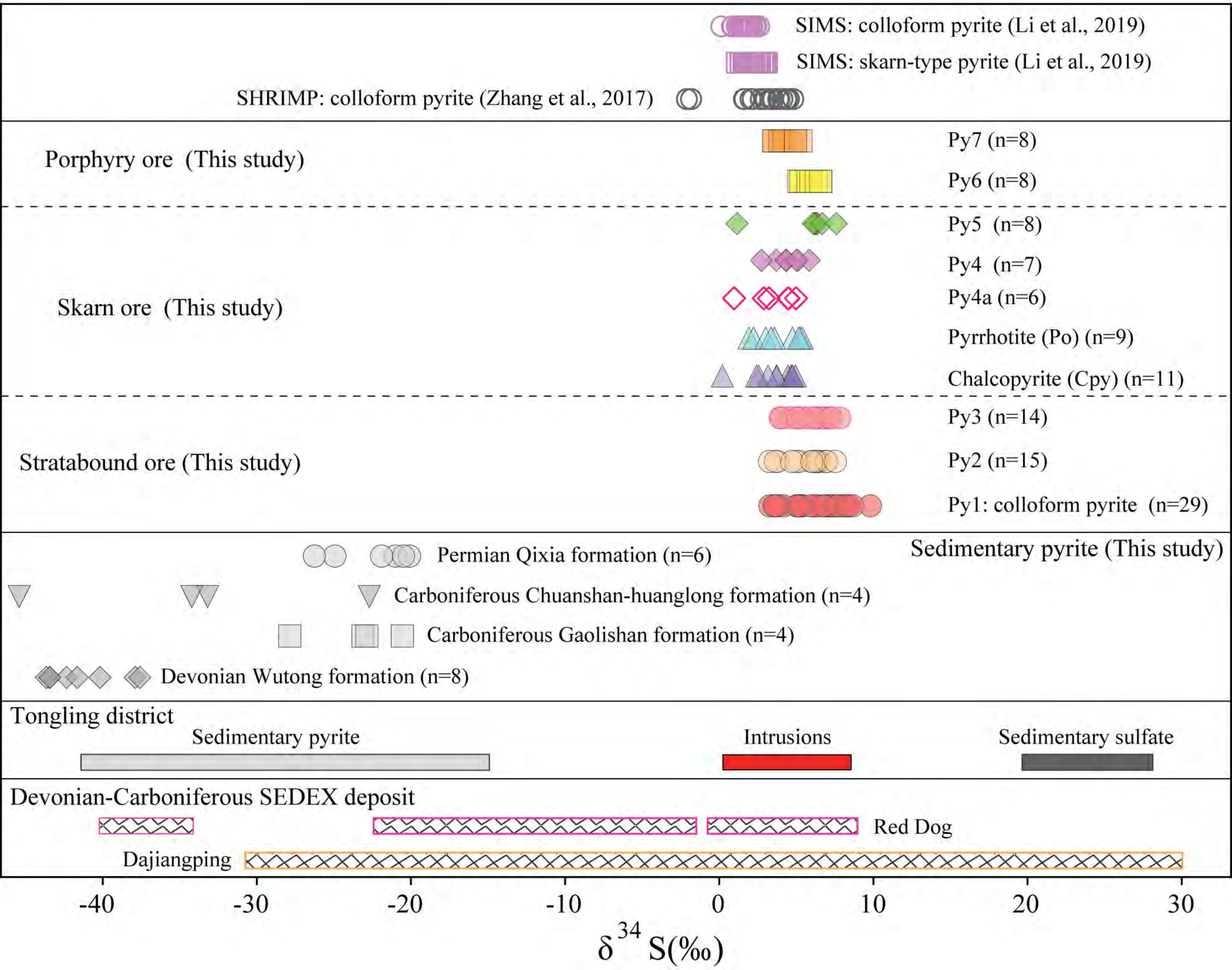
SIMS: colloform pyrite (Li et al., 2019)
SIMS: skarn-type pyrite (Li et al., 2019)
SHRIMP: colloform pyrite (Zhang et al., 2017)
Porphyry ore (This study)
Py7 (n=8)
Py6 (n=8)
Skarn ore (This study)
Py5 (n=8)
Py4 (n=7)
Py4a (n=6)
Pyrrhotite (Po) (n=9)
Chalcopyrite (Cpy) (n=11)
Stratabound ore (This study)
Py3 (n=14)
Py2 (n=15)
Py1: colloform pyrite (n=29)
Sedimentary pyrite (This study)
Permian Qixia formation (n=6)
Carboniferous Chuanshan-huanglong formation (n=4)
Carboniferous Gaolishan formation (n=4)
Devonian Wutong formation (n=8)
Tongling district
Sedimentary pyrite
Intrusions
Sedimentary sulfate
Devonian-Carboniferous SEDEX deposit
Red Dog
Dajiangping
-40
-30
-20
-10
0
10
20
30
δ 34 S(‰)

Figure 12

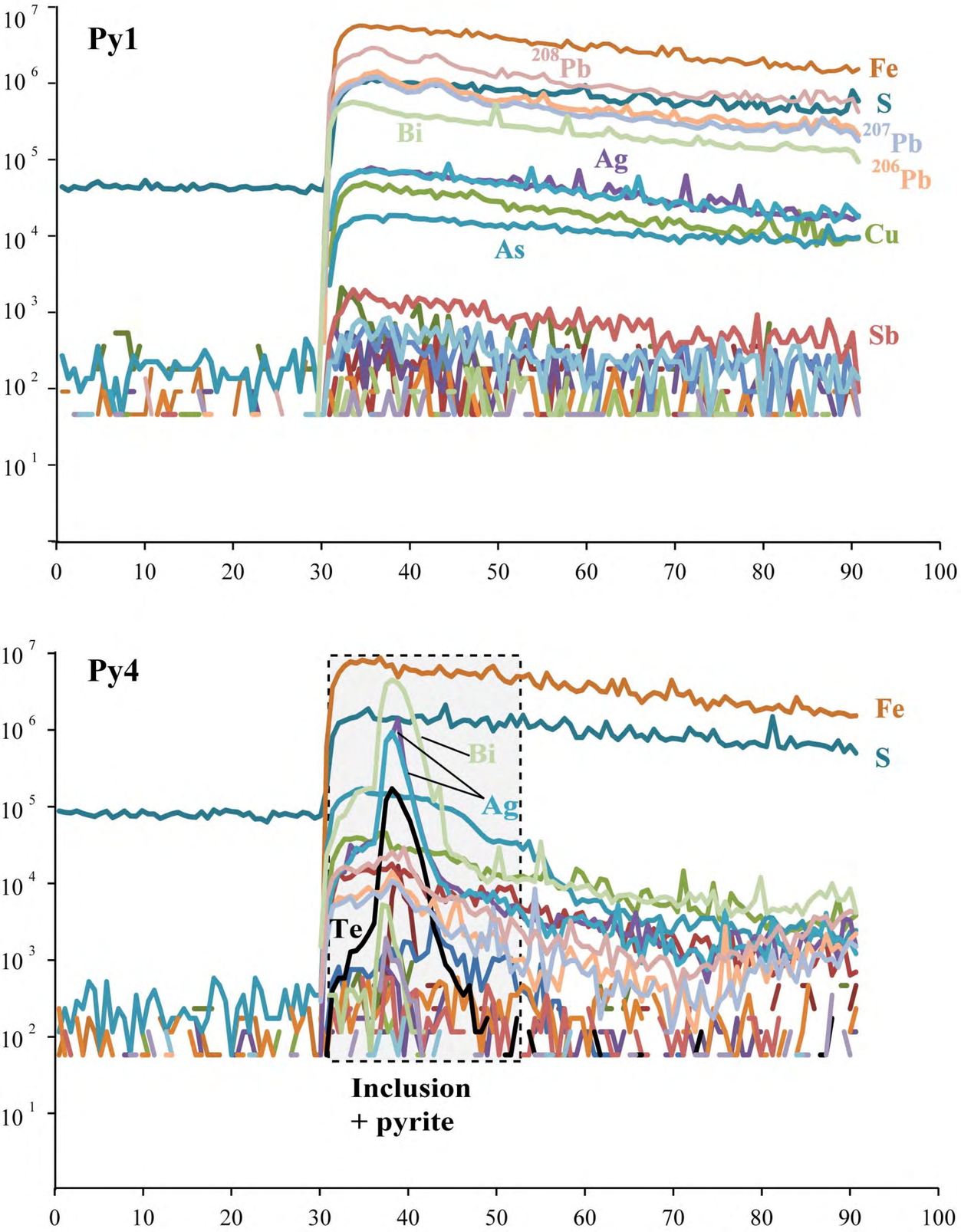
Py1
208Pb
Fe
S
Bi
207Pb
Ag
206Pb
As
Cu
Sb
10 7
10 6
10 5
10 4
10 3
10 2
10 1
0
10
20
30
40
50
60
70
80
90
100

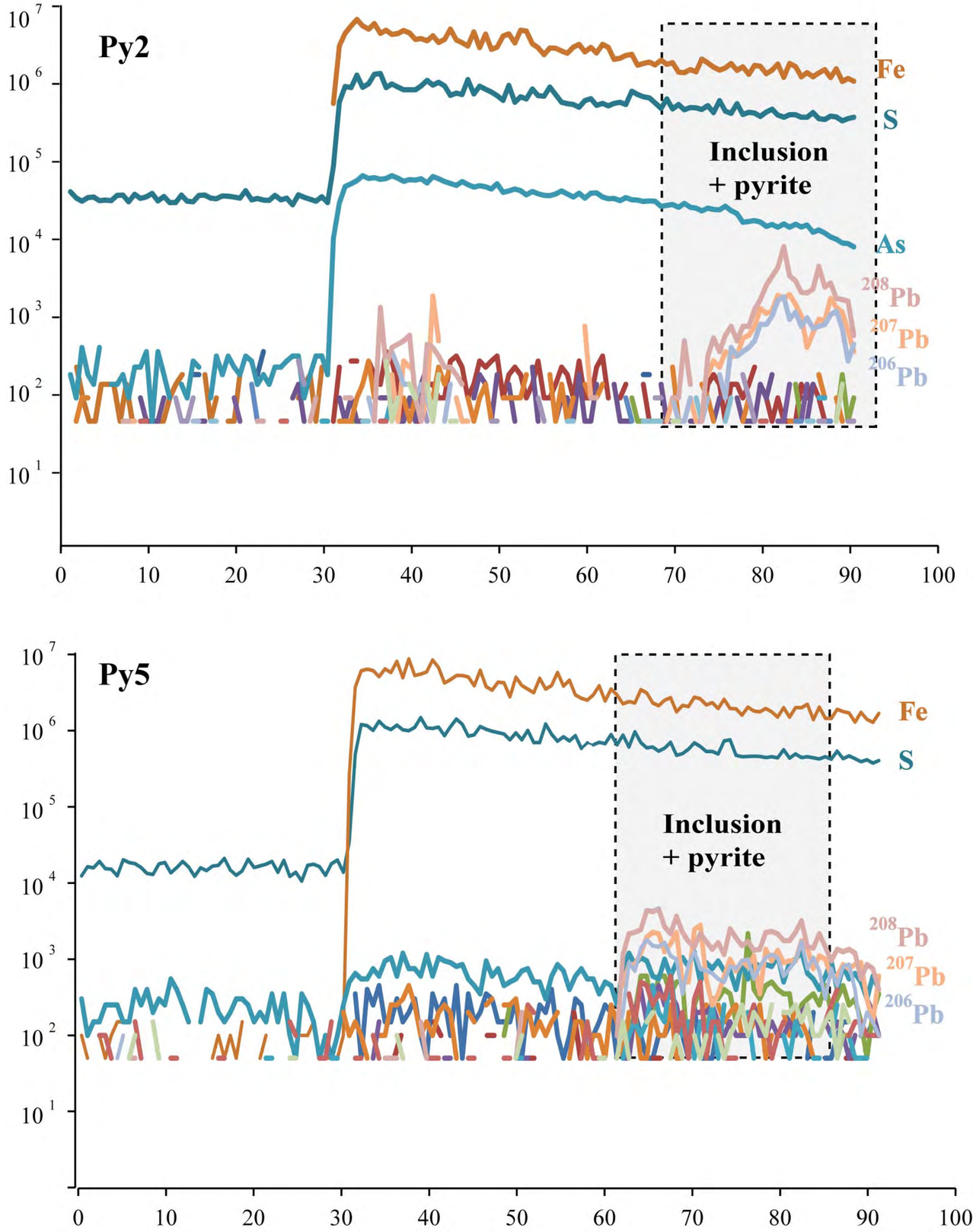
Py2
Fe
S
Inclusion
+ pyrite
As
208Pb
207Pb
206Pb
10 7
10 6
10 5
10 4
10 3
10 2
10 1
0
10
20
30
40
50
60
70
80
90
100

Py4
Fe
S
Bi
Ag
Te
Inclusion
+ pyrite
10 7
10 6
10 5
10 4
10 3
10 2
10 1
0
10
20
30
40
50
60
70
80
90
100

Py5
Fe
S
Inclusion
+ pyrite
208Pb
207Pb
206Pb
10 7
10 6
10 5
10 4
10 3
10 2
10 1
0
10
20
30
40
50
60
70
80
90
100

Figure 13

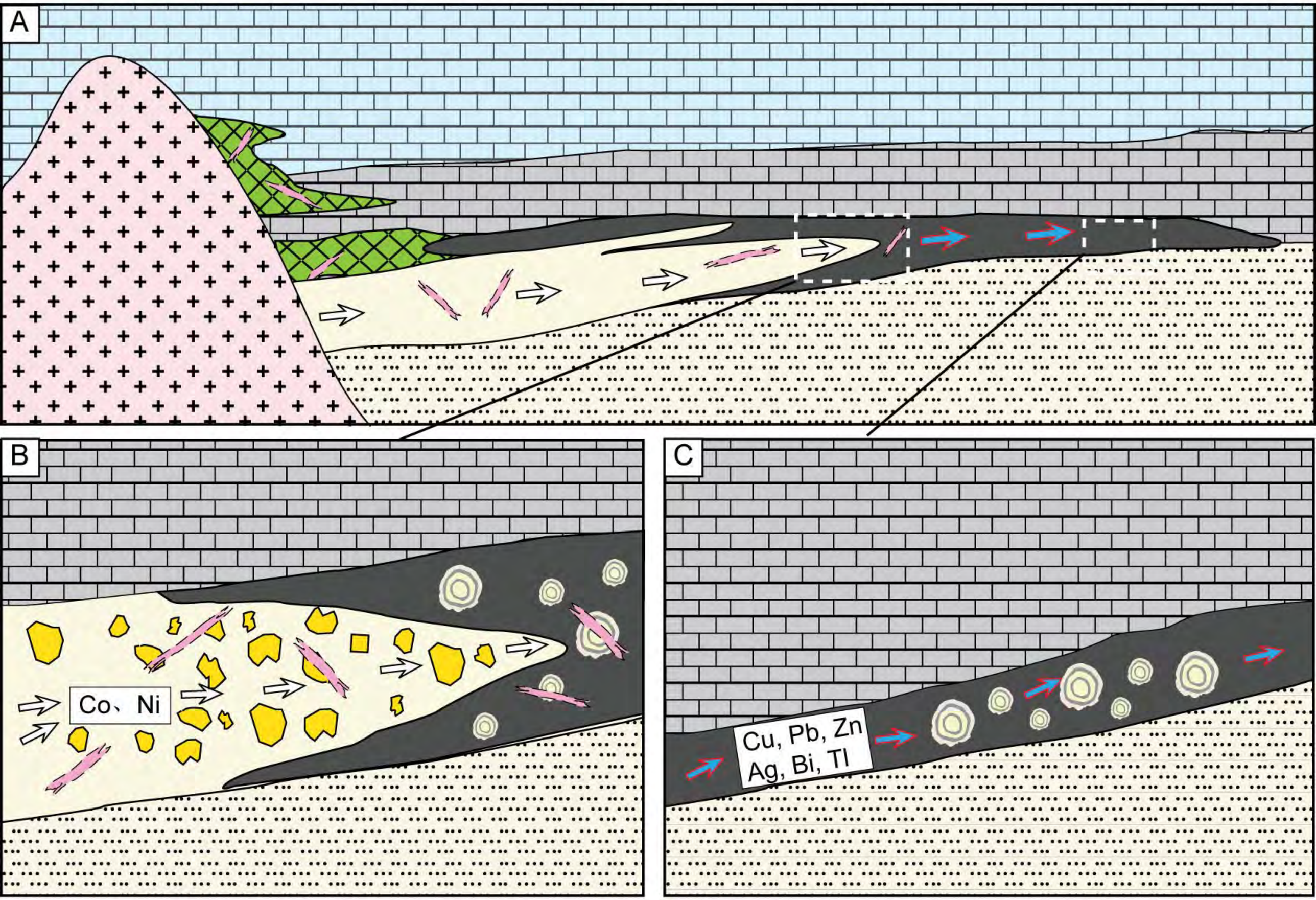
A
B
C
Co、Ni
Cu, Pb, Zn
Ag, Bi, Tl
Permian limestone
Late Carboniferous limestone & dolomite limestone
Devonian sandstone
Jitou stock
(Quartz monzodiorite)
Magmatic-hydrothermal fluid
of early sulfide stage
Magmatic-hydrothermal fluid
of later sulfide stage
Skarn
Colloform pyrite ore
Coarse-grained pyrite ore
Fine pyrite-chalcopyrite vein

Figure 14

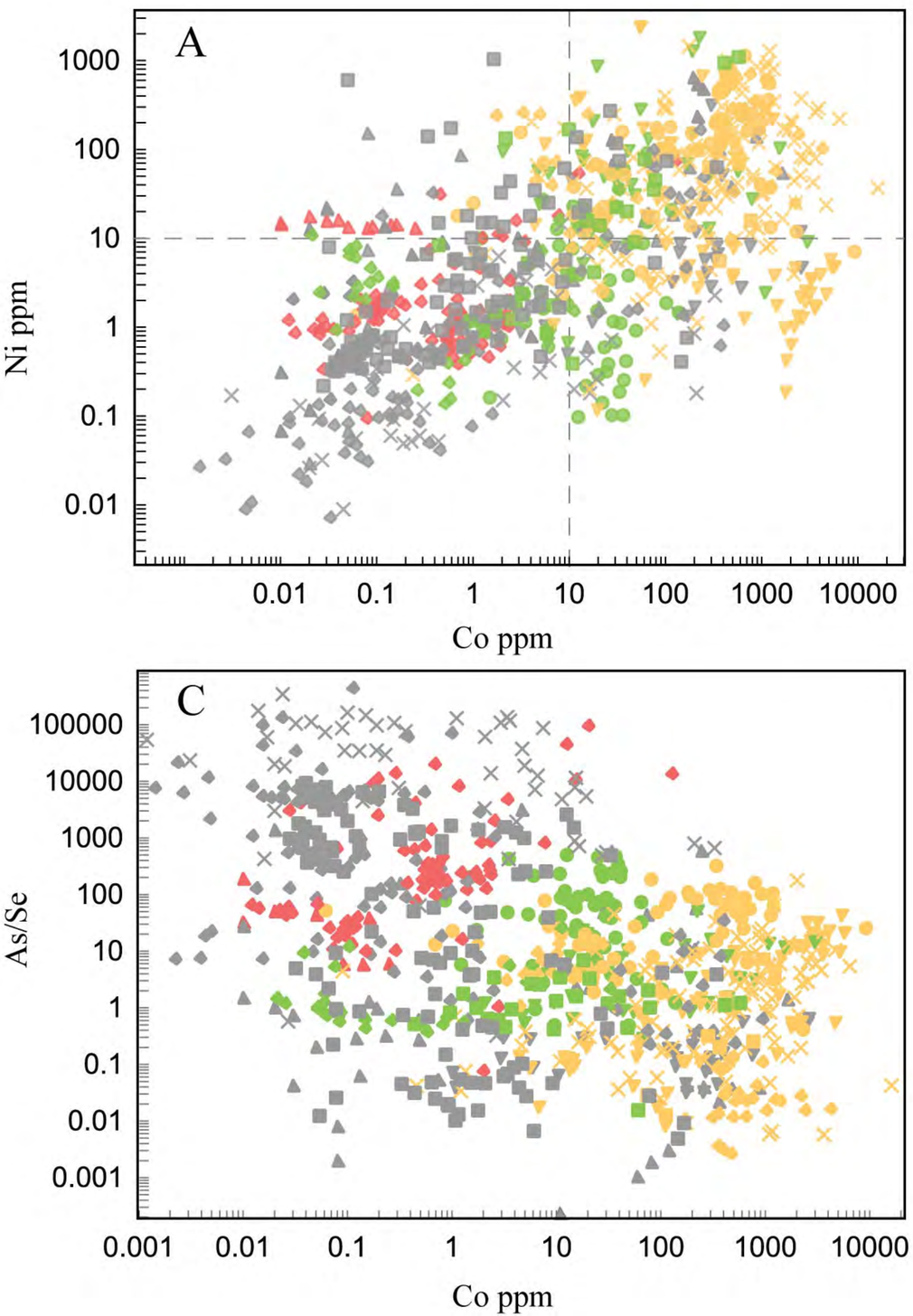
A
Ni ppm
1000
100
10
1
0.1
0.01
0.01
0.1
1
10
100
1000
10000
Co ppm
C
As/Se
100000
10000
1000
100
10
1
0.1
0.01
0.001
0.001
0.01
0.1
1
10
100
1000
10000
Co ppm

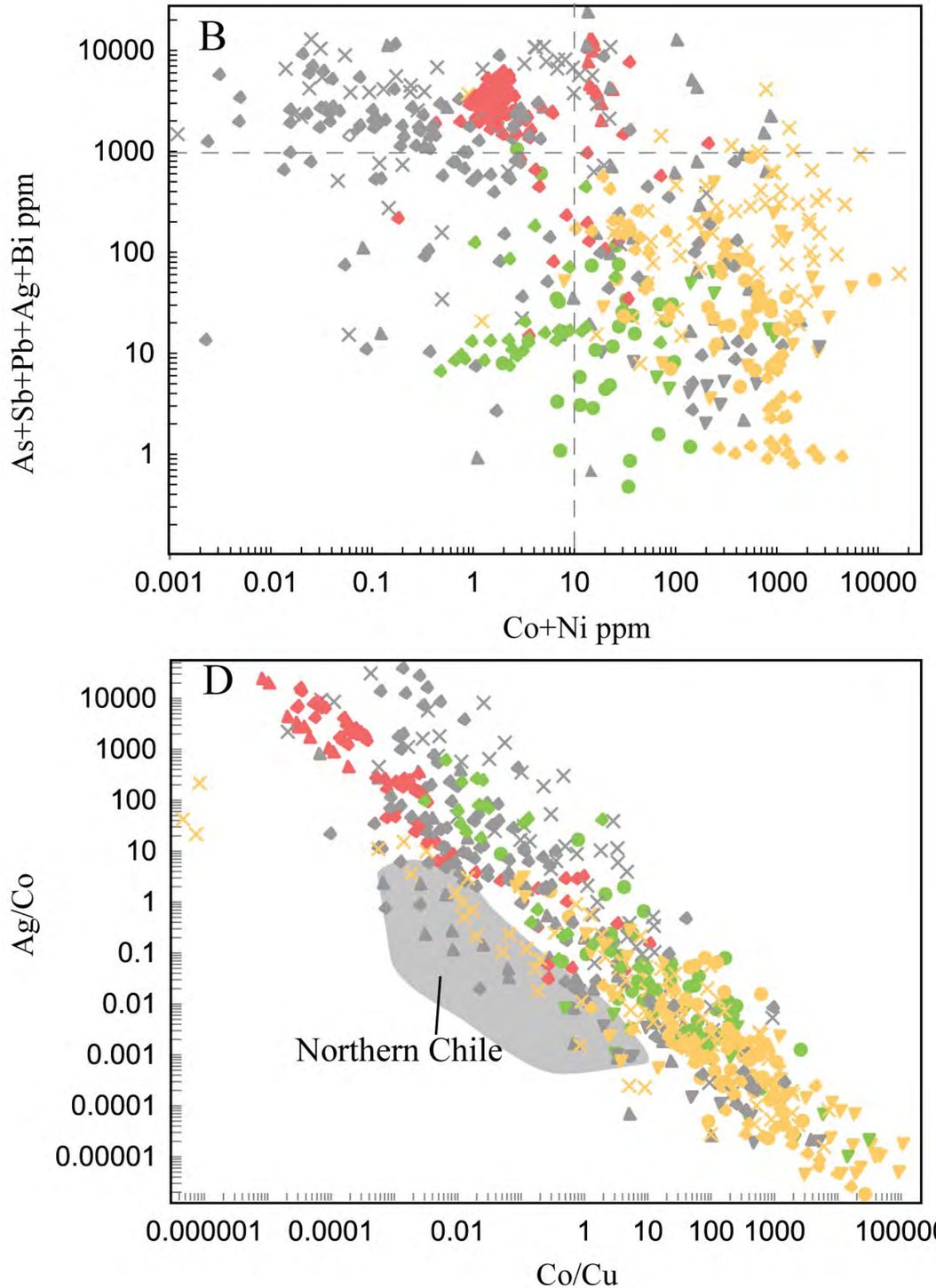
B
As+Sb+Pb+Ag+Bi ppm
10000
1000
100
10
1
0.001
0.01
0.1
1
10
100
1000
10000
Co+Ni ppm
D
Ag/Co
10000
1000
100
10
1
0.1
0.01
0.001
0.0001
0.00001
Northern Chile
0.000001
0.0001
0.01
1
10
100
1000
100000
Co/Cu
Stratabound ore
Xinqiao
Xinqiao (colloform pyrite)
Dongguashan
Taoyuan
Jingjiwo
Jingjiwo (colloform pyrite)
Chengmenshan
Skarn ore
Xinqiao
Dongguashan
Fenghuangshan
Chengmenshan
Porphyry ore
Xinqiao
Dongguashan
Fenghuangshan
Shujiadian
Chengmenshan